

Multidimensional stability analysis of the phase-field method for fracture with a general degradation function and energy split.

Miguel Arriaga¹ · Haim Waisman¹

Received: 28 December 2016 / Accepted: 2 June 2017 / Published online: 17 June 2017
© Springer-Verlag GmbH Germany 2017

Abstract A local physical stability criterion for multidimensional fracture problems modeled by the phase field method is developed and studied. Stability analysis provides a rigorous mathematical way to determine the onset of an unstable damage growth and fracture of the structure. In this work, stability is determined by examining the roots of a characteristic equation that arise when a linear perturbation technique is applied to the instantaneous partial differential equation system in a general viscoplastic material. It is shown that such analysis is not limited to a particular degradation function or energy split and could therefore be applied to a wide range of cases. Numerical results are presented to verify the theoretical predictions assuming quadratic and cubic degradation functions. Additionally we show that this stability criterion can be directly expanded to 2D with robust mesh-insensitive predictive capabilities with respect to crack nucleation and path. Several numerical examples are presented to verify these results.

Keywords Phase field · Fracture · Instability · Linear perturbation

1 Introduction

The phase field method has gained significant attention in recent years due to its ability to solve difficult moving boundary problems. For example, it has been successfully applied

to a wide range of problems such as solidification or liquefaction [1–3], solid-state phase transformation [4,5], martensitic transformation [6,7], dislocation dynamics [8], grain growth [9,10], twinning [11–13] among others.

In this work, the phase-field methodology is used to model fracture, which has been studied extensively in the literature [14–25]. Here, cracks are approximated as diffused damage zones that depend on a length-scale parameter l_0 [16,26], as depicted in Fig. 1.

Since the crack is approximated by a continuous function, special discontinuous shape functions or enrichments as the one required for discrete description of fracture, can completely be avoided. Additionally, complex crack patterns such as branching and coalescence can easily be captured with this approach. The phase-field formulation is regarded by some as a subset of damage mechanics and is closely related to gradient damage methods [27–29].

Loss of stability is often associated with structural collapse, extensive damage or decreased reliability of the numerical results. In quasi-static cases, phenomena like bifurcation due to non-associated flow law [30–32] will affect the stability and lead to poor numerical performance, often requiring more advanced stepping procedures (e.g. the arc-length method [33]) and regularization techniques to prevent mesh dependency in localization phenomena [34–37]. For dynamic cases, stability often determines the transition of a homogeneous solution into a non-homogeneous solution, for example in a thermo-mechanical shearband localization problem [38–40].

Local stability analysis provides important information and insight into the deformation state associated with the distribution of localization regions and the onset of material failure. Some work reported in the literature upscale localization processes to a coarser scale by injecting a strong displacement discontinuity with cohesive surfaces at the

✉ Haim Waisman
waisman@civil.columbia.edu

¹ Department of Civil Engineering and Engineering Mechanics, Columbia University, 610 Seeley W. Mudd Building, 500 West 120th Street, Mail Code 4709, New York, NY 10027, USA

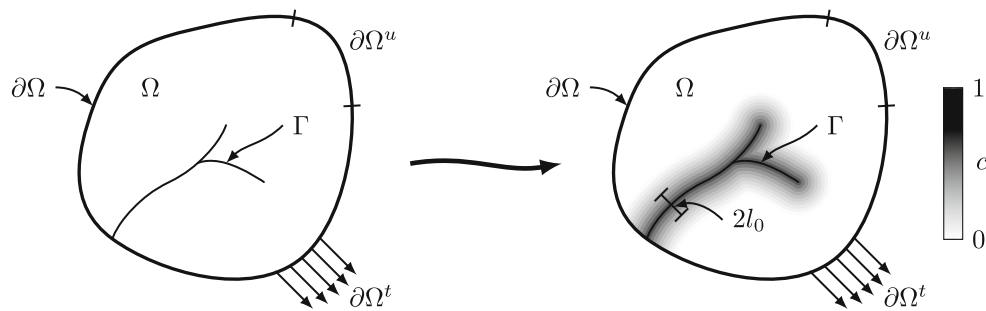


Fig. 1 Schematic depiction of a solid Ω with a crack discontinuity Γ . In the phase-field formulation the crack is described by the field c where a black color corresponds to a fully damaged material ($c = 1$)

and a white color corresponds to a fully intact material ($c = 0$). The l_0 parameter controls the width of the process zone

moment that a local instability is detected. For example such multiscale approach has been reported for shearbands [41] and fracture [42], among others [43–46].

One of the most important features that control the behavior of the phase field method, is the so-called degradation function. This function is used to degrade a chosen component of the elastic strain energy (e.g. the energy associated with tension) and is typically associated with the current state of damage (i.e. the phase-field parameter).

The degradation function, denoted by $m(c)$, can be chosen arbitrarily as long as it satisfies the conditions necessary to observe Gamma convergence [27] and boundedness of the fracture force [20].

In the bulk of the work done on phase field methods, a quadratic degradation function is typically used as it is the only one for which Γ -convergence has been demonstrated [22]. However, in recent years other degradation functions have been developed [47]. For example a cubic degradation function has been suggested by [48] and was shown to provide some advantages like closer resemblance to an elastic-brittle behavior as expected and obtained by traditional methods and reduction of the mild degradation that occurs away from the crack.

In this work we study the stability behavior of the phase-field method applied to elasticity, rate-independent plasticity and visco-plasticity with isotropic hardening. This work generalizes the work on stability analysis of the phase field method [49] in the extension to multidimensional problems with complex crack patterns and bifurcations, and the generalization to generic degradation functions (here we analyze and compare quadratic and cubic functions). Stability is determined by examining the roots of a characteristic equation that arise due to a linear perturbation technique applied to the instantaneous partial differential equation (PDE) system. Instability is then defined if the real part of one of the roots becomes positive, since each root corresponds to the growth-rate of a perturbation, and a positive value means that such perturbation will grow exponentially in time.

A linear perturbation analysis is more general than the loss of ellipticity criterion determined by analysis of the acoustic tensor, since for rate-dependent materials the equations remain elliptical and this criterion may not be appropriate, as argued in the literature [50,51]. On the other hand, the linear perturbation method was successfully applied to various localization problems including rate-dependent materials, for example in the formation and propagation of shear bands in metals [38,39,52–54].

This work is structured as follows. In Sect. 2 the governing equations are presented and the problem is stated. In Sect. 3 the stability criterion for a general degradation function is derived based on the linear perturbation method applied to the 1D continuous PDE system. Additionally, the analysis is expanded to a multidimensional version of the elastic problem. In Sect. 4 we present numerical simulations verifying the analytical predictions and in Sect. 5 we investigate the behavior of this approach in various 2D examples. Finally, the conclusions are presented in Sect. 6.

2 Problem statement

Consider an elastic-viscoplastic solid subjected to loads and appropriate boundary conditions. The phase field method is used to model its fracture assuming small strains.

The governing equations of this problem are given by [55]

$$\text{Momentum:} \quad \rho \ddot{u}_i = \sigma_{ij,j} + b_i \quad (1)$$

Damaged Elastic Const. Law:

$$\sigma_{ij} = C_{ijkl}^{elas} \varepsilon_{kl}^e + [m(c) - 1] \frac{\partial W^+}{\partial \varepsilon_{ij}^e} \quad (2)$$

Strain-Displacement:

$$\varepsilon_{ij}^e = \frac{1}{2} (u_{i,j} + u_{j,i}) - \varepsilon_{ij}^p \quad (3)$$

Phase-Field:

$$\rho \theta_c \ddot{c} = G_c 2l_0 c_{,ii} - \frac{G_c}{2l_0} c - \frac{\partial m}{\partial c} (W^+ + P^+) \quad (4)$$

Inelastic Const. Law:

$$\dot{\gamma}^p = g(\bar{\sigma}, \bar{\gamma}^p) \geq 0 \tag{5}$$

In the momentum Eq. (1), ρ is the density, u_i the displacement field, σ_{ij} the stress tensor and b_i the body force. In the damaged elastic constitutive Eq. (2), C_{ijkl}^{elas} is the fourth-order elastic constitutive tensor, ε_{ij}^e is the elastic strain tensor, W^+ is the component of the elastic strain energy degraded by damage and $m(c)$ is the degradation function that relates the phase-field parameter c with the damage in the solid.

An additive decomposition of the strain in Eq. (3) is used, in which the plastic strain tensor is given by

$$\varepsilon_{ij}^p = \int_0^{t_0} \frac{3}{2} \frac{g(\bar{\sigma}, \bar{\gamma}^p)}{\bar{\sigma}} S_{ij} dt' \tag{6}$$

where t' is a dummy integration parameter, t_0 is the current time. The function $g(\bar{\sigma}, \bar{\gamma}^p)$ is the flow law used to compute the equivalent plastic strain rate ($\dot{\gamma}^p$).

The effective stress $\bar{\sigma}$ is a conjugate quantity to the equivalent plastic strain ($\bar{\gamma}^p$) and is given by

$$\bar{\sigma} = \sqrt{\frac{3}{2} S_{ij} S_{ij}} \tag{7}$$

where the deviatoric stress S_{ij} is

$$S_{ij} = \sigma_{ij} - \frac{1}{3} \sigma_{kk} \delta_{ij} \tag{8}$$

and δ_{ij} is the Kronecker delta.

Note that the damaged elastic constitutive Eq. (2), is obtained by considering that the total degraded elastic strain energy is given by the sum of two factors $W^- + m(c)W^+$ where W^- is the component of the strain energy that is not affected by the fracture behavior (typically the compression component of the strain) and W^+ is the component of the strain energy that is degraded by $m(c)$. Hence, the stress can in general be expressed as

$$\sigma_{ij} = \frac{\partial W^-}{\partial \varepsilon_{ij}^e} + m(c) \frac{\partial W^+}{\partial \varepsilon_{ij}^e} \tag{9}$$

which rearranging and noting that $C_{ijkl}^{elas} \varepsilon_{kl}^e = \frac{\partial W^-}{\partial \varepsilon_{ij}^e} + \frac{\partial W^+}{\partial \varepsilon_{ij}^e}$ yields the damaged elastic constitutive Eq. (2).

Equation (4) is the typical phase field equation [15, 16, 19–21], where c denotes the extent of damage or the phase-field parameter, θ_c is the so called micro-inertia, G_c corresponds to the fracture energy of the material (i.e. the critical energy release rate which is a material parameter) and l_0 is the process zone parameter, where $2l_0$ roughly corresponds to the

dimension of the process zone, also known as the characteristic length (See Fig. 1). The phase-field parameter c ranges from 0 to 1, where the value of 0 corresponds to an uncracked state and the value of 1 to a fully cracked state. When the parameter $l_0 \rightarrow 0$, the approximation of the fracture energy by the phase-field method converges to the fracture energy of a discontinuous crack [56], provided that sufficient mesh refinement within this zone is employed. Finally, P corresponds to the total stored inelastic energy and P^+ is the component of the stored inelastic energy that is degraded by damage and consequently contributes to fracture. Note that in the current work we neglect the effect of micro-inertia by setting $\theta_c = 0$.

The total stored inelastic energy is given by [55, 57]

$$P = \int_0^{t_0} (1 - \chi) \sigma_{ij} \dot{\varepsilon}_{ij}^p dt \tag{10}$$

where χ is the so called Taylor–Quinney coefficient [58] that gives the fraction of the total plastic work ($\sigma_{ij} \dot{\varepsilon}_{ij}^p$) that is dissipated into heat, and t_0 is the current time. The definition of P^+ depends on the micro-structural mechanisms that are contributing to the generation of fracture surface. As a simplifying assumption, P^+ can be defined as being a constant fraction of the plastic work, which yields

$$P^+ = \int_0^{t_0} \chi^f \sigma_{ij} \dot{\varepsilon}_{ij}^p dt \tag{11}$$

where χ^f , similarly to Taylor–Quinney, is the fraction of the total plastic work that goes into fracture generation. Naturally the sum $\chi + \chi^f$ must not exceed the value of 1, i.e. $\chi^f \leq 1 - \chi$.

The inelastic constitutive Eq. (5) depends specifically on the chosen flow law. In this work we assume a flow law of the form

$$\bar{\sigma} = Q(\bar{\gamma}^p) R(\dot{\bar{\gamma}}^p) \tag{12}$$

which is used for many popular material models such as Johnson Cook [59] or Litonski [60].

The material considered for the numerical results is a modified 4340 Steel with a Johnson–Cook constitutive law [59] without thermal softening as given in (13). The material parameters of this steel are presented in Table 1 and the modified Johnson–Cook parameters are given in Table 2. These modifications served to enhance the differences between different strain-rates to better verify the theoretical predictions. The parameters used for the phase-field modeling are the Critical Fracture Energy (G_c) and the Process Zone Parameter (l_0).

Table 1 Material properties for 4340 Steel

Property name	Symbol	Value	Unit
Mass density	ρ	7830	kg/m ³
Young’s modulus	E	200	GPa
Poisson’s ratio	ν	0.29	-
Shear modulus	μ	77.5	GPa
Critical fracture energy	G_c	12.5	kJ/m ²
Process zone parameter	l_0	50	μm

Table 2 Johnson–Cook parameters for 4340 Steel

Property name	Symbol	Value	Unit
Yield shear stress	A_s	1300.0	MPa
Shear stress hardening parameter	B_s	700.0	MPa
Strain hardening parameter	N	0.26	-
Strain-rate hardening parameter	c_h	0.1	-
Reference strain-rate	$\dot{\gamma}_r^p$	1.0	10 ³ /s

$$\tau = \left[A_s + B_s (\gamma^p)^N \right] \left[1 + c_h \ln \left(\frac{\dot{\gamma}^p}{\dot{\gamma}_r^p} \right) \right] \tag{13}$$

Finally, the boundary conditions needed to solve the system are

$$u_i = \bar{u}_i \quad \text{on} \quad \partial\Omega^u \tag{14}$$

$$n_j \cdot \sigma_{ij} = \bar{t}_i \quad \text{on} \quad \partial\Omega^t \tag{15}$$

$$n_i \cdot H_i = 0 \quad \text{on} \quad \partial\Omega \tag{16}$$

where \bar{u}_i and \bar{t}_i are the prescribed boundary displacements and tractions, respectively. H_i is the micro-traction defined as $H_i = G_c 2l_0 c_{,i}$ [55]. The entire boundary is given by $\partial\Omega = \partial\Omega^u \cup \partial\Omega^t$.

This model considers small strains, and additionally neglects thermal effects. At $t = 0$ the system is considered to be unstressed, undamaged and undeformed.

3 Stability analysis

3.1 1D characteristic equation

Recalling the linear perturbation method used for a stability analysis process, a scalar function $f(x)$ can be expanded in a Taylor Series around some value x_0 . Taking only the first order term, one can linearize the function and express it as

$$f(x) \approx f_0 + \delta f \tag{17}$$

where

$$f_0 = f(x_0) \quad \text{and} \quad \delta f = \left(\frac{\partial f(x)}{\partial x} \Big|_{x=x_0} \right) \delta x \tag{18}$$

Hence, in our case we assume a perturbation of all independent variables in the PDE system $(u, c, \sigma, \bar{\gamma}^p)$. For simplicity any of the fields will be represented by x and we assume that the perturbations are periodic functions of time and space, that is

$$\delta x = \delta \hat{x} e^{\omega t + iky} \tag{19}$$

where ω corresponds to the growth-rate of the perturbation and k the corresponding wave-number. The variables t, y and i correspond to time, space and the imaginary unit $\sqrt{-1}$, respectively.

We study a 1D pure tension formulation of the problem stated in Sect. 2 with the linear perturbation method and obtain a characteristic equation. In this formulation the normal stress is represented by τ and the strain by γ . A monotonic loading is assumed to avoid elastic unloading.

The perturbed equations obtained by this procedure are

$$\rho \delta \ddot{u} = \delta \tau' \tag{20}$$

$$\delta \tau = E \left(m_0 \delta \gamma^e + \gamma_0^e \frac{\partial m_0}{\partial c} \delta c \right) \tag{21}$$

$$\delta \gamma^e + \delta \gamma^p = \delta u' \tag{22}$$

$$\begin{aligned} \delta c = & \alpha \delta c'' - \beta \frac{\partial^2 m_0}{\partial c^2} W_0^+ (1 + f_0^p) \delta c \\ & - \beta \frac{\partial m_0}{\partial c} \left(\frac{\partial W_0^+}{\partial \gamma^e} \delta \gamma^e + \frac{\partial P_0^+}{\partial \gamma^p} \delta \gamma^p \right) \end{aligned} \tag{23}$$

$$\delta \tau = \frac{\partial \tau}{\partial \gamma^p} \delta \gamma^p + \frac{\partial \tau}{\partial \dot{\gamma}^p} \delta \dot{\gamma}^p \tag{24}$$

where

$$f_0^p = P_0^+ / W_0^+ \tag{25}$$

Recall that, as noted in (18), a variable with a subscript 0 corresponds to the value of that variable (or its derivatives) at the solution point being perturbed. For example, m_0 corresponds to the value of the degradation function $m(c)$ at the current equilibrium point.

Resolving all spatial and temporal differentiations, the independent variables can be eliminated by manipulation of (20)-(24), which will yield a cubic normalized characteristic equation of the form

$$C_0 + C_1 \tilde{\omega} + C_2 \tilde{\omega}^2 + C_3 \tilde{\omega}^3 = 0 \tag{26}$$

where C_i are the coefficients of the polynomial characteristic equation that depend on material parameters (E, G_c, \dots) and the current values of the solution (m_0, W_0^+, P_0^+, \dots). The reader is referred to Appendix A for the specific values of C_i .

Subsequently, we apply the Routh-Hurwitz stability conditions to the characteristic equation. These state that a third order polynomial will be stable, i.e. all its roots are on the negative real half-plane, if the following conditions are met:

$$C_i > 0 \quad i = 0, 1, 2, 3 \quad \text{and} \quad C_1 C_2 > C_3 C_0 \quad (27)$$

Therefore, a necessary and sufficient condition for instability is that at least one of these inequalities will not be satisfied. Analyzing each condition individually leads to a final criterion for the existence of a root of the characteristic equation with positive real part, (i.e. instability), as follows

$$\frac{\phi}{\theta} > \phi_c \quad (28)$$

with $\phi = 2\beta W_0^+, \theta = 1 + \alpha k^2$. The parameter $\alpha = 4l_0^2$ is referred to as the gradient coefficient and corresponds to the square of the characteristic length of the model. As mentioned before, $2l_0$ defines the width of the diffused crack, which means that as l_0 decreases, the value of α also decreases, making the crack narrower. The parameter $\beta = \frac{2l_0}{G_c}$, relates the amount of energy that contributes to fracture with the critical fracture energy G_c (a material property). Therefore, the term $\beta(W^+ + P^+)$ quantifies the amount of energy with respect to G_c driving the evolution of the smeared crack and serves as the source for the phase-field term.

The critical instability energy is defined as

$$\phi_c = \frac{1}{\frac{1}{m_0} \left(\frac{\partial m_0}{\partial c} \right)^2 - \frac{1+f_0^p}{2} \frac{\partial^2 m_0}{\partial c^2}} \quad (29)$$

The limiting value of θ for the earliest onset of instability is $\theta = 1$, which leads to the expression for instability

$$\phi > \phi_c \Rightarrow \phi - \phi_c > 0 \quad (30)$$

The reader is referred to [49] for additional details.

3.2 Application to cubic degradation function

A cubic formulation for the degradation function was proposed by [48]

$$m(\bar{c}) = (3-s)\bar{c}^2 + (s-2)\bar{c}^3 \quad (31)$$

with $\bar{c} = 1 - c$ in our formulation. The parameter s controls the behavior of the degradation function at the onset of

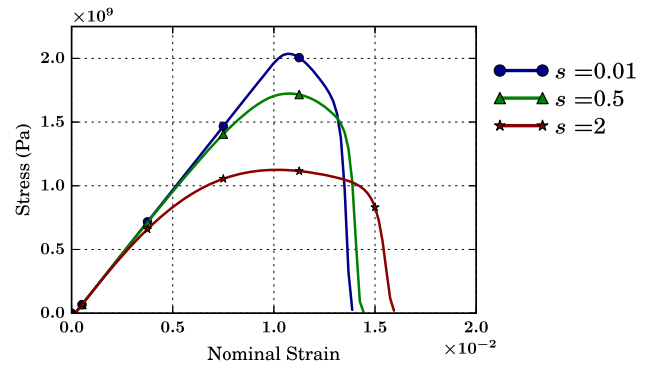


Fig. 2 Stress-strain curves for different values of s in an elastic material. Geometry and material parameters are given in the results section and in Appendix B

damage, i.e. $\frac{\partial m}{\partial c} \Big|_{c=0} = -s$. A value of $s = 2$ degenerates the cubic equation into the quadratic one. The cubic degradation function allows for a more “linear” behavior of the stress-strain curve before the peak stress, as opposed to the quadratic function.

In Fig. 2, the behavior of the stress-strain curve of an elastic material is demonstrated. Here one can see that the peak value of stress increases as the s parameter goes from 2, equivalent to a quadratic degradation function, to 0. Note that the smaller the value of s , the closer the stress-strain curve will be to a linear behavior before the peak stress.

Plugging the degradation function back onto (29), the condition for instability is obtained

$$\phi > \phi_c = \frac{1/(3-s)}{\frac{(2+3a\bar{c})^2}{1+a\bar{c}} - (1+f_0^p)(1+3a\bar{c})} \quad (32)$$

where $a = \frac{s-2}{3-s}$. Note that f_0^p is the ratio between the plastic work and the elastic work that contribute to fracture, as given in (25).

Figure 3 represents the degradation function ($m(c)$) and the critical energy (ϕ_c) as a function of c and s . The cubic degradation function with $s = 0$ gives a horizontal tangent at $c = 0$. In practice this presents problems from the numerical point of view and a sufficiently small number should be used instead of 0. If $s = 2$ (quadratic) then the stability condition is independent of c as confirmed by other methods in the literature [15, 18]. However, for any other value of s , the stability condition will be dependent on c , as can be seen in Fig. 3b.

Despite the results of Fig. 3b, we are only really interested in the value of ϕ_c at the critical point, i.e. at the moment when the solution becomes unstable due to $\phi = \phi_c$. Therefore we compute and depict in Fig. 4 the critical phase-field parameter (c_c) and the critical energy (ϕ_c) as a function of s and f^p for the cubic degradation function at the moment of instability. The value of c_c is obtained by considering the phase-field

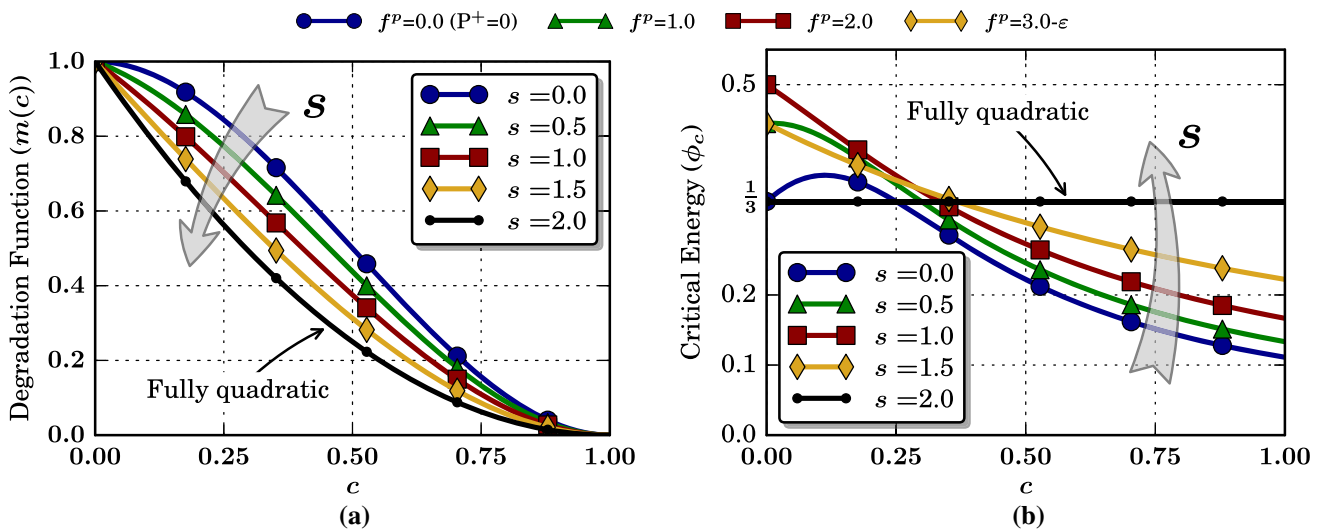


Fig. 3 **a** Degradation function $m(c)$ (left) and **b** critical energy ϕ_c (right) for the cubic formulation (31) with respect to c and s . The fully quadratic result in elasticity ($P^+ = 0$) recovers the critical values of $\phi_c = 1/3$

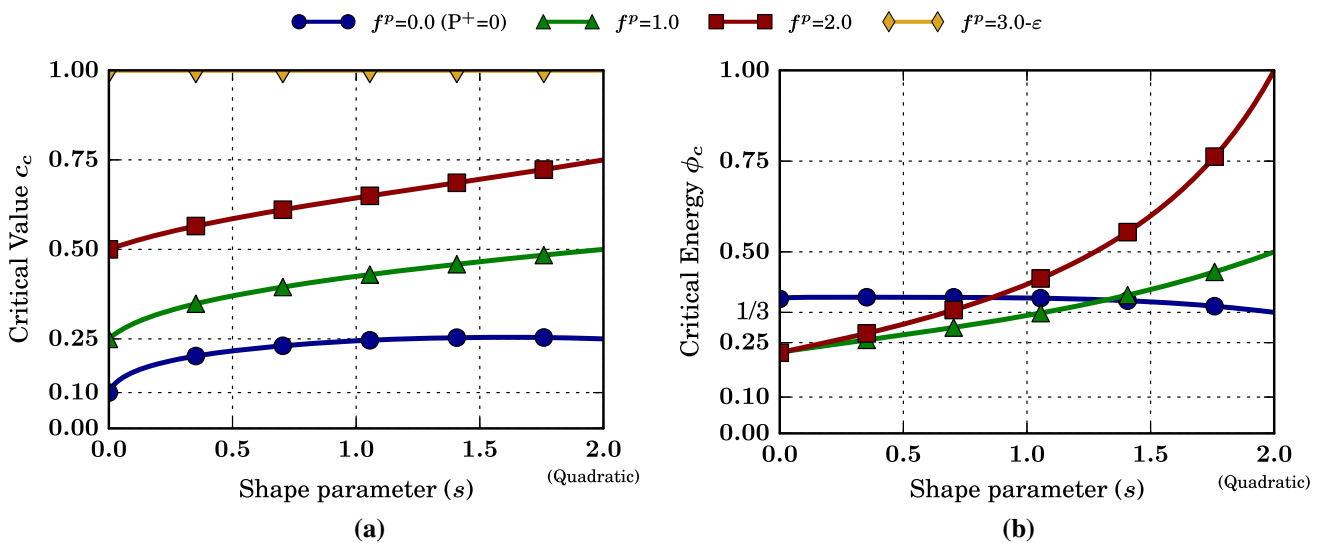


Fig. 4 **a** Critical phase-field parameter c_c (left) and **b** critical energy ϕ_c (right) for the cubic degradation function (31) with respect to s and f^p . The fully quadratic result in elasticity ($P^+ = 0$) recovers the critical values of $c_c = 0.25$ and $\phi_c = 1/3$. [15, 18, 48]

Eq. (4) in a uniform state ($c_{,ii} = 0$) and setting $\phi = \phi_c$ as follows

$$c = -\beta W^+ \frac{\partial m}{\partial c} (1 + f_0^p) \Rightarrow \phi_c(c_c) = -\frac{2c_c}{\frac{\partial m(c_c)}{\partial c} (1 + f_0^p)} \quad (33)$$

plugging ϕ_c from Eq. (32) solving for c_c results in an expression for c_c with a cubic degradation function (see Appendix C).

Additionally, by plugging the resulting c_c back into ϕ_c (32) we can compute the value of the critical energy at the moment of instability. The value of critical energy for $f^p = 3$

is not represented as it corresponds to the limit case where the energy goes to infinity. This becomes clear by setting \bar{c} to zero in Eq. (32). In the limit case of $s = 2$ (i.e. quadratic degradation) in elasticity, the critical values of $c_c = 1/4$ and $\phi_c = 1/3$ are obtained, as expected from earlier literature results [15, 18, 25, 48].

3.3 Stability criterion by eigenvalue analysis of the discrete system

The stability of a problem can also be analyzed from a numerical perspective by making use of the concept of Lyapunov stability where a local eigenvalue analysis of a particular par-

tion of the element Jacobian matrix (or Tangent Stiffness Matrix) is analyzed, as presented in [39].

As [61] stated: “arbitrarily slow perturbations in a rate-dependent solid can only grow from quasistatic solutions.” By arbitrarily slow perturbations it is understood that perturbations with small but positive growth-rate or the first eigenvalue which crosses the real half plane and becomes positive, correspond to the onset of instability.

In the current dynamic fracture model, to obtain the residual equations we first define the weak form of the governing equations by multiplying each equation in (1)–(5) by its corresponding weight function, integrating over the problem domain and using integration by parts where necessary.

$$r_u = \int_{\Omega} w_i^u \rho \ddot{u}_i \, d\Omega + \int_{\Omega} w_{i,j}^u \sigma_{ij} \, d\Omega - \int_{\Gamma} w_i^u \sigma_{ij} n_j \, d\Gamma \tag{34}$$

$$r_{\sigma} = \int_{\Omega} w_{ij}^{\sigma} \sigma_{ij} \, d\Omega - \int_{\Omega} w_{ij}^{\sigma} \left[C_{ijkl}^{elas} \varepsilon_{kl}^e + [m(c) - 1] \frac{\partial W^+}{\partial \varepsilon_{ij}^e} \right] \, d\Omega \tag{35}$$

$$r_c = \int_{\Omega} w^c c \, d\Omega + \int_{\Omega} w_{,i}^c 4l_0^2 c_{,i} \, d\Omega + \int_{\Omega} w^c \frac{2l_0}{G_c} \frac{\partial m}{\partial c} (W^+ + P^+) \, d\Omega \tag{36}$$

$$r_{\bar{\gamma}^p} = \int_{\Omega} w^{\bar{\gamma}^p} \dot{\bar{\gamma}}^p \, d\Omega - \int_{\Omega} w^{\bar{\gamma}^p} g(T, \bar{\sigma}, \bar{\gamma}^p) \, d\Omega \tag{37}$$

Note that the Strain-Displacement equation is not explicitly included in the weak form, but it is implicitly taken into account when computing the elastic strain in the Damaged Elastic Constitutive Law.

Accounting for the Babuska-Brezzi condition [62–64] in mixed finite element formulations, the shape functions for each field must be chosen with care. To this end, we choose C^0 shape functions for displacement and phase-field parameter, and piecewise continuous functions for the stress and equivalent plastic strain.

The residual equations can be grouped into a residual vector \mathbf{r} and a solution vector \mathbf{x} with displacements, stress, phase-field and plastic strain as

$$\mathbf{x} = \begin{bmatrix} u_i \\ c \\ \sigma_{ij} \\ \bar{\gamma}^p \end{bmatrix} \quad \mathbf{r} = \begin{bmatrix} r_u \\ r_c \\ r_{\sigma} \\ r_{\bar{\gamma}^p} \end{bmatrix} \tag{38}$$

The coupled nonlinear problem can then be stated as

$$-\mathbf{r}(\mathbf{x}_0, \dot{\mathbf{x}}_0, \ddot{\mathbf{x}}_0) = \mathbf{M} \cdot \delta \ddot{\mathbf{x}} + \mathbf{C} \cdot \delta \dot{\mathbf{x}} + \mathbf{K} \cdot \delta \mathbf{x} \tag{39}$$

where $\mathbf{r}(\mathbf{x}, \dot{\mathbf{x}}, \ddot{\mathbf{x}})$ is the vector with the residual of each equation in the set of governing equations of the problem and \mathbf{x} is the solution vector which contains all field variables being solved for ($u_i, c, \sigma_{ij}, \bar{\gamma}^p$). $\mathbf{M} \cdot \delta \ddot{\mathbf{x}}$, $\mathbf{C} \cdot \delta \dot{\mathbf{x}}$ and $\mathbf{K} \cdot \delta \mathbf{x}$ are the obtained by computing the Gâteaux differential [65] of the residual(\mathbf{r}) in the $\delta \ddot{\mathbf{x}}$, $\delta \dot{\mathbf{x}}$ and $\delta \mathbf{x}$ directions as follows

$$\mathbf{M} \cdot \delta \ddot{\mathbf{x}} = d_{\delta \ddot{\mathbf{x}}} \mathbf{r}(\mathbf{x}, \dot{\mathbf{x}}, \ddot{\mathbf{x}}) = \left. \frac{d}{d\epsilon} \mathbf{r}(\mathbf{x}, \dot{\mathbf{x}}, \ddot{\mathbf{x}} + \epsilon \delta \ddot{\mathbf{x}}) \right|_{\epsilon=0} \tag{40}$$

$$\mathbf{C} \cdot \delta \dot{\mathbf{x}} = d_{\delta \dot{\mathbf{x}}} \mathbf{r}(\mathbf{x}, \dot{\mathbf{x}}, \ddot{\mathbf{x}}) = \left. \frac{d}{d\epsilon} \mathbf{r}(\mathbf{x}, \dot{\mathbf{x}} + \epsilon \delta \dot{\mathbf{x}}, \ddot{\mathbf{x}}) \right|_{\epsilon=0} \tag{41}$$

$$\mathbf{K} \cdot \delta \mathbf{x} = d_{\delta \mathbf{x}} \mathbf{r}(\mathbf{x}, \dot{\mathbf{x}}, \ddot{\mathbf{x}}) = \left. \frac{d}{d\epsilon} \mathbf{r}(\mathbf{x} + \epsilon \delta \mathbf{x}, \dot{\mathbf{x}}, \ddot{\mathbf{x}}) \right|_{\epsilon=0} \tag{42}$$

The Jacobian matrix is then built by approximating the rate and acceleration of the solution increment ($\delta \dot{\mathbf{x}}$ and $\delta \ddot{\mathbf{x}}$) with a Newmark-beta[66] time-integration scheme such that (39) becomes

$$\mathbf{J} \cdot \delta \mathbf{x} = -\mathbf{r}(\mathbf{x}_0, \dot{\mathbf{x}}_0, \ddot{\mathbf{x}}_0) \tag{43}$$

where the Jacobian matrix \mathbf{J} is given by

$$\mathbf{J} = \begin{bmatrix} \mathbf{M}_{uu}^* & 0 & \mathbf{K}_{u\sigma}^L & 0 \\ \mathbf{G}_{cu} & \mathbf{K}_{cc}^L + \mathbf{G}_{cc} & \mathbf{G}_{c\sigma} & \mathbf{G}_{c\bar{\gamma}^p} \\ \mathbf{K}_{\sigma u}^L & \mathbf{G}_{\sigma c} & \mathbf{K}_{\sigma\sigma}^L & \mathbf{G}_{\sigma\bar{\gamma}^p} \\ 0 & 0 & \mathbf{G}_{\bar{\gamma}^p\sigma} & \mathbf{C}_{\bar{\gamma}^p\bar{\gamma}^p}^* + \mathbf{G}_{\bar{\gamma}^p\bar{\gamma}^p} \end{bmatrix} \tag{44}$$

with the superscript (*) indicating that the matrix has been scaled by the constants that result from the time-integration scheme used.

The quasi-static finite element formulation of the system can be acquired by considering the \mathbf{K} component of the Jacobian matrix, i.e. the component of the Jacobian matrix that is affecting the non-rate terms of the governing equations. Hence, the matrix \mathbf{K} is given by

$$\mathbf{K} = \begin{bmatrix} 0 & 0 & \mathbf{K}_{u\sigma}^L & 0 \\ \mathbf{G}_{cu} & \mathbf{K}_{cc}^L + \mathbf{G}_{cc} & \mathbf{G}_{c\sigma} & \mathbf{G}_{c\bar{\gamma}^p} \\ \mathbf{K}_{\sigma u}^L & \mathbf{G}_{\sigma c} & \mathbf{K}_{\sigma\sigma}^L & \mathbf{G}_{\sigma\bar{\gamma}^p} \\ 0 & 0 & \mathbf{G}_{\bar{\gamma}^p\sigma} & \mathbf{G}_{\bar{\gamma}^p\bar{\gamma}^p} \end{bmatrix} \tag{45}$$

where $\mathbf{K} = \mathbf{K}^L + \mathbf{G}$ represents the sum of the stiffness matrices associated with linear material behavior such as elasticity and thermal diffusion (\mathbf{K}^L) and the tangent stiffness matrices associated with material non-linear behavior (\mathbf{G}). Note that the matrix \mathbf{K} is nonsymmetric and will potentially lead to complex eigenvalues. We refer to [55,57] for additional details on this formulation, which was implemented in the finite element software FEAP [67].

Therefore, the stability condition based on the numerical approximation is obtained when there exists an eigenvalue of \mathbf{K} with a positive real part, i.e.

$$\text{Re} [\text{eig}(\mathbf{K})] > 0 \tag{46}$$

The main advantage of this process is that it is straight forward to apply and will be as accurate as the FEM approximation. An implicit assumption of this method is that the

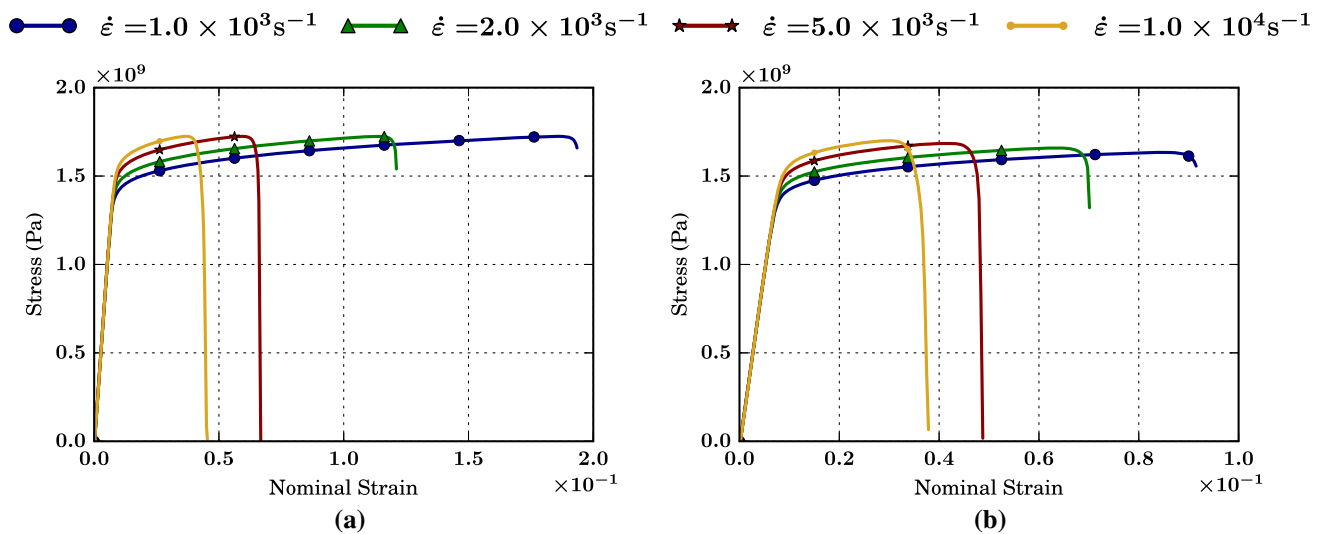


Fig. 5 Stress-strain curves for different values of strain-rate in an visco-plastic material with $s = 0.5$ **a** $P^+ = 0$ **b** $P^+ \neq 0$ with $\chi^f = 0.01$

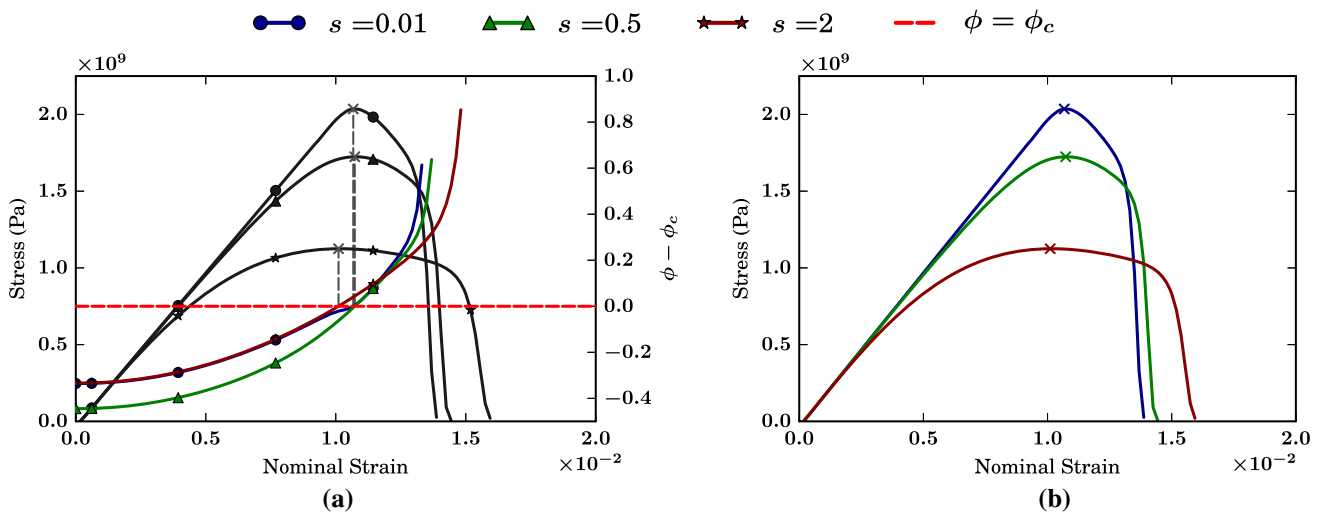


Fig. 6 Stability analysis of an elastic material for different values of s in the degradation function. The bar is loaded at $\dot{\epsilon} = 5.0^3 s^{-1}$. Figure 6a shows that when the colored lines that correspond to the quantity $\phi - \phi_c$ (black) and stability condition (colored lines). **b** Onset of instability marked on stress-strain curves

the stress will be at its peak value. Figure 6b shows a simplified plot with only the stress-strain curves and the instability points **a** stress-strain (black) and stability condition (colored lines). **b** Onset of instability marked on stress-strain curves

values for the wave-length of the perturbation are limited to permutations of the degrees of freedom within the element discretization. In other words, the wave-lengths are locked to the element size. Nonetheless, we neglect the influence of this effect since, as mentioned earlier, the limit case is given by $k \rightarrow 0$, which corresponds to an infinitely large wave-length of the perturbation (i.e. uniform solution), which can be easily captured by the Finite Element discretization of the problem.

While this approach will be shown in the next section to agree well with both analytical criteria for shear bands and fracture, one limitation of this method is that it does not distinguish between the types of failure modes

as is clearly obtained with the analytical criterion. Another drawback of the spectral method is its higher computational burden, as it requires a solution of an eigenvalue problem at each element and will slow down the analysis, which might be significant in large scale parallel computations.

4 Numerical results in 1D

The 1D formulation used in this section is an idealized version of the Split-Hopkinson bar experiment [68–70]. Consider a 1D steel rod subject to a set of tension loads

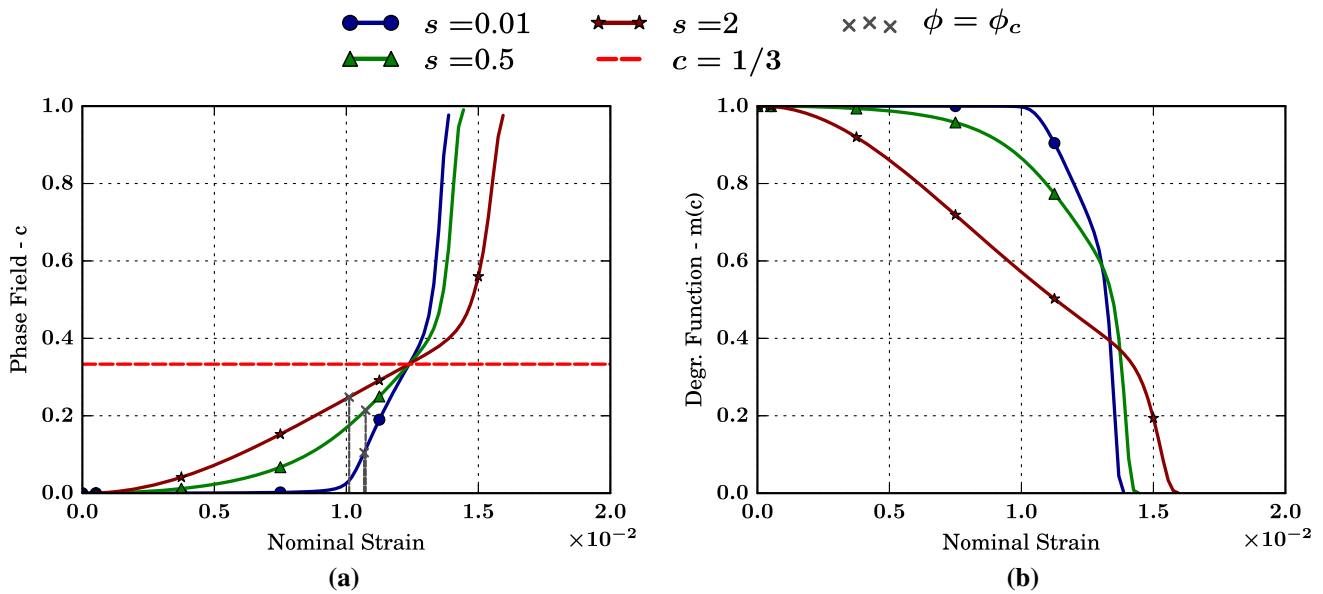


Fig. 7 Evolution of the phase field and degradation for different values of s as a function of the nominal strain. As the value of s decreases away from the quadratic degradation function $s = 2$, the growth of the phase-field parameter c and the reduction of the degradation function

$m(c)$ will be delayed. This means that a smaller s value reduces the non-linearity before the instability point, giving the stress-strain curve a more linear behavior before the formation of the crack **a** phase field parameter (c) **b** degradation function ($m(c)$)

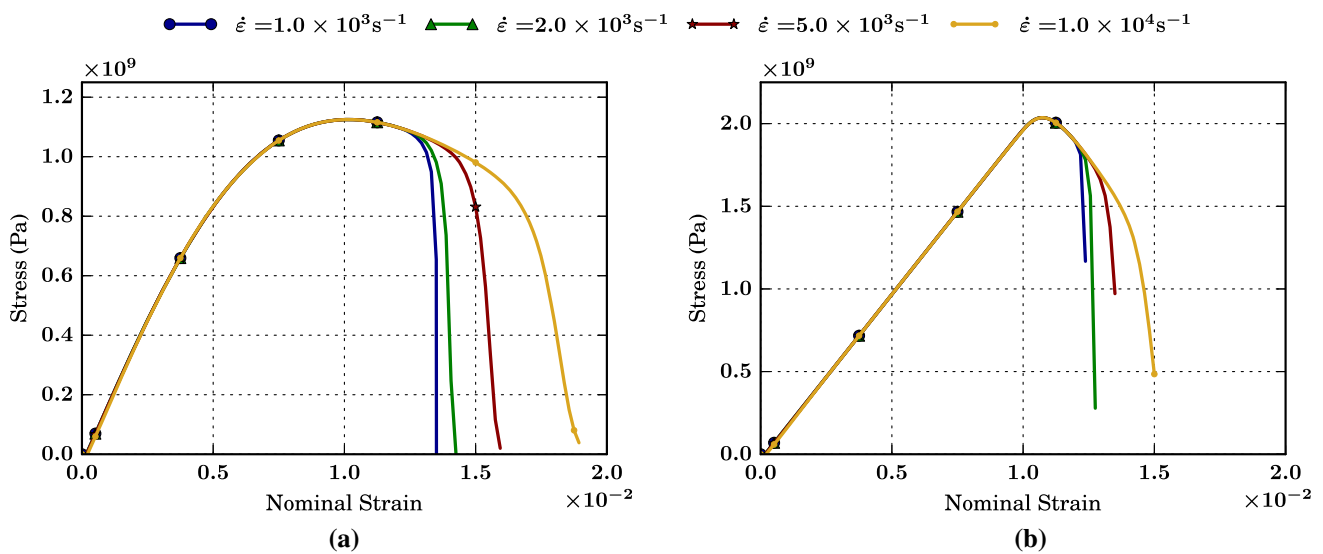


Fig. 8 Stress-strain curves for different values of strain-rate in an elastic material **a** $s = 2$ (quadratic) **b** $s = 0.01$ (cubic)

corresponding to a multitude of strain rates, which are modeled using a displacement control approach. A finer discretization of the bar is employed in the center to better capture the steep gradients associated with the crack while a coarser mesh is employed further away. A Johnson–cook type material law is employed excluding thermal effects and a small imperfection that reduces the yield stress and the critical fracture energy is applied in the center. A detailed description of the discretization and mate-

rial parameters of the model can be found in Sect. 2 and Appendix B.

Figure 5 depicts the behavior of the stress-strain curve of a visco-plastic material with and without the contribution of P^+ , where a $\chi^f = 0.01$ was used for the case with $P^+ \neq 0$. In both cases, as the rate of deformation increases, the peak value of stress occurs for a smaller value of strain due to the rate-hardening behavior of the material. When $P^+ = 0$, the value of the peak stress is the same for all cases since soften-

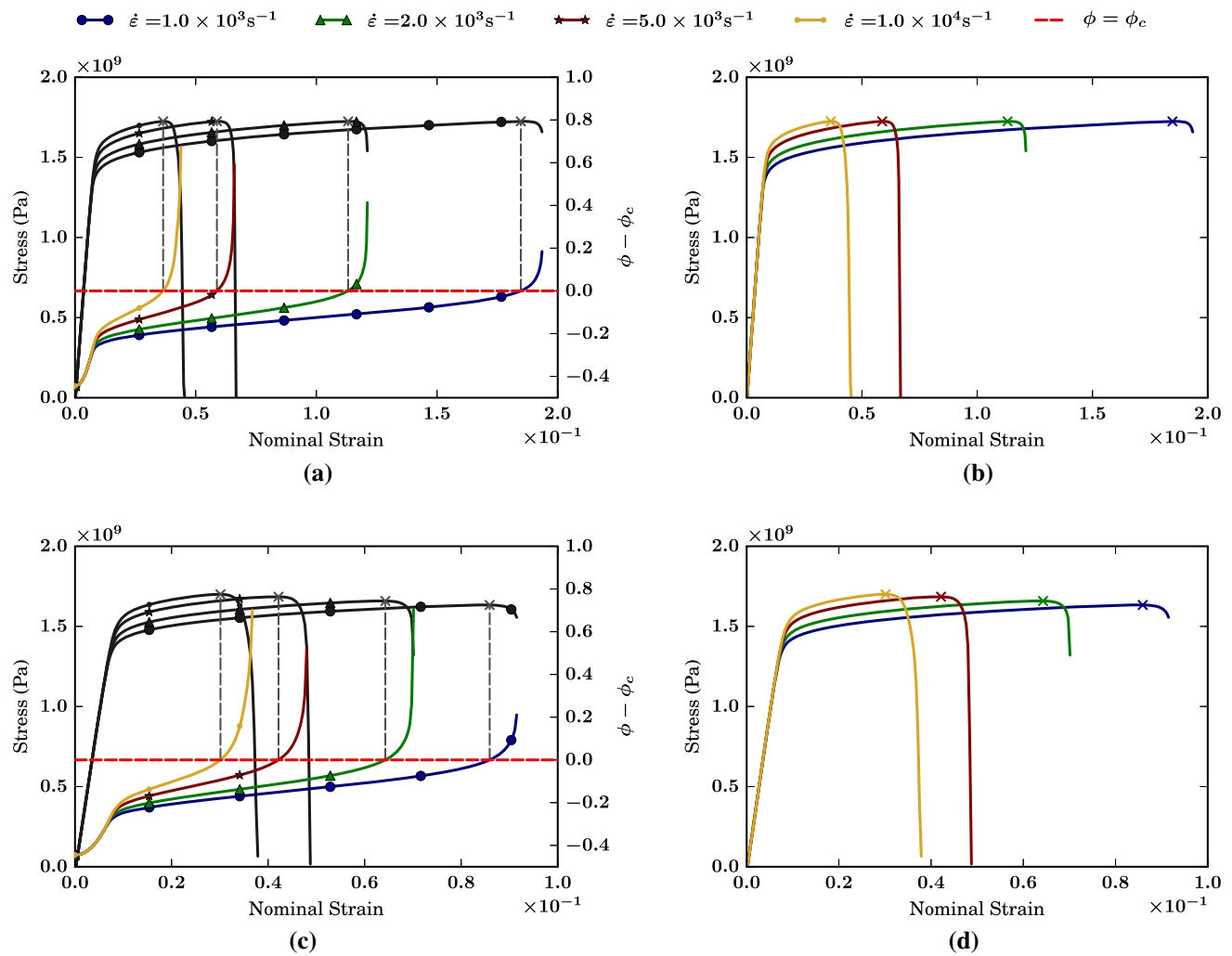


Fig. 9 Stability analysis of an elastic material for different strain rates, with $s = 0.5$. **a** and **c** show the stress-strain (*black lines*) and the stability condition (*colored lines*), with $P^+ = 0$ and $P^+ = 0$, respectively. When the colored lines that correspond to the quantity $\phi - \phi_c$ cross the value

of zero, i.e. the instability condition (Eq. 30) is met, then the stress will be at its peak value. Figures **b** and **d** show the correspondent simplified plots with only the stress-strain curves and the instability points

ing is only due to the phase-field degradation, which in turn only depends on the elastic energy. On the other hand, when the phase field is also affected by the accumulated inelastic work that contributes to fracture, i.e. $P^+ \neq 0$, then the critical stress and the critical strain are reduced, causing an earlier onset fracture.

4.1 Comparison between degradation functions in an elastic material

In Fig. 6 the stability condition (30) is plotted for different values of s in an elastic material loaded at strain-rate of $\dot{\epsilon} = 5.0^3 s^{-1}$. It can be observed that the stability condition accurately recovers the peak stress, which confirms the analytical result.

When the problem is homogeneous, the value of ϕ is only a function of the nominal strain. Therefore, before the formation of the crack, the differences in $\phi - \phi_c$ between the models are strictly due to the difference between the values of ϕ_c . This explains why the value of $\phi - \phi_c$ is the same for $s = 0.01$ and $s = 2$, since (as can be observed in Fig. 3b) the value of ϕ_c is very similar in both cases.

For the cubic case with $s = 0$ there is an interesting phenomenon where it can be observed an increase of ϕ_c that delays the instability point. This is consistent with the behavior of the curve with $s = 0$ in Fig. 3b that initially grows for small values of c .

In addition, since the value of ϕ_c for $s = 0$ stays close to $1/3$ almost up to the instability point, it is expected that the value of c remains close to zero during this time. This can be confirmed by observing the value of c as a function

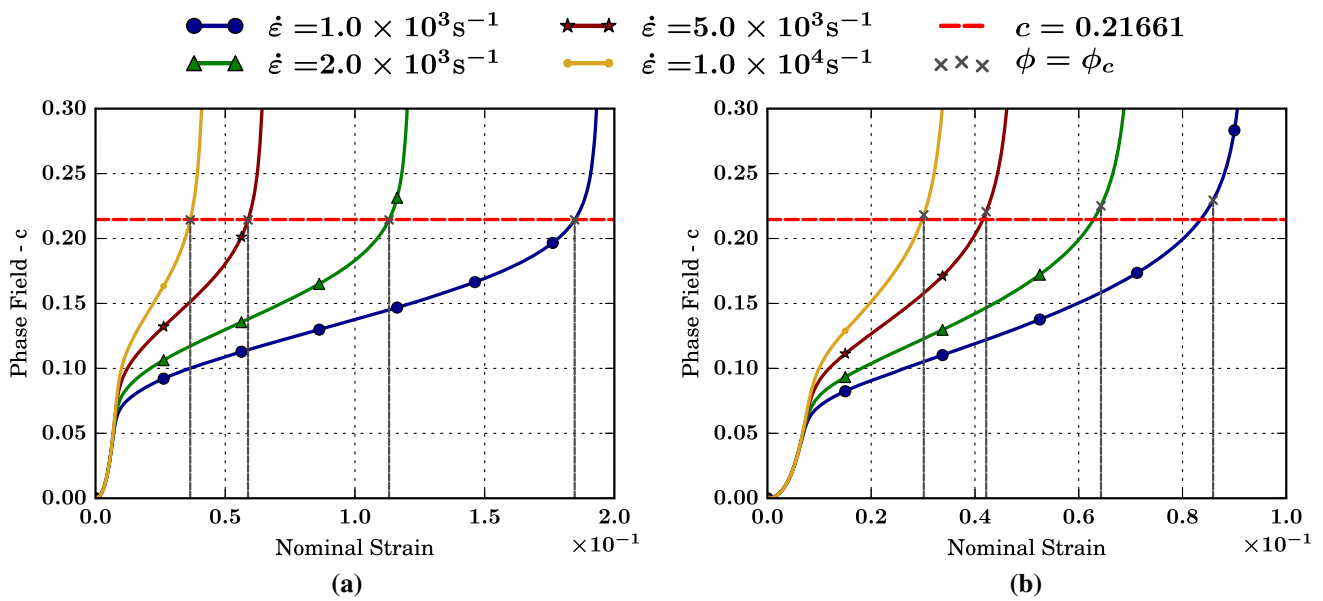


Fig. 10 Evolution of the phase field parameter (c) in a visco-plastic material **a** $P^+ = 0$ **b** $P^+ \neq 0$

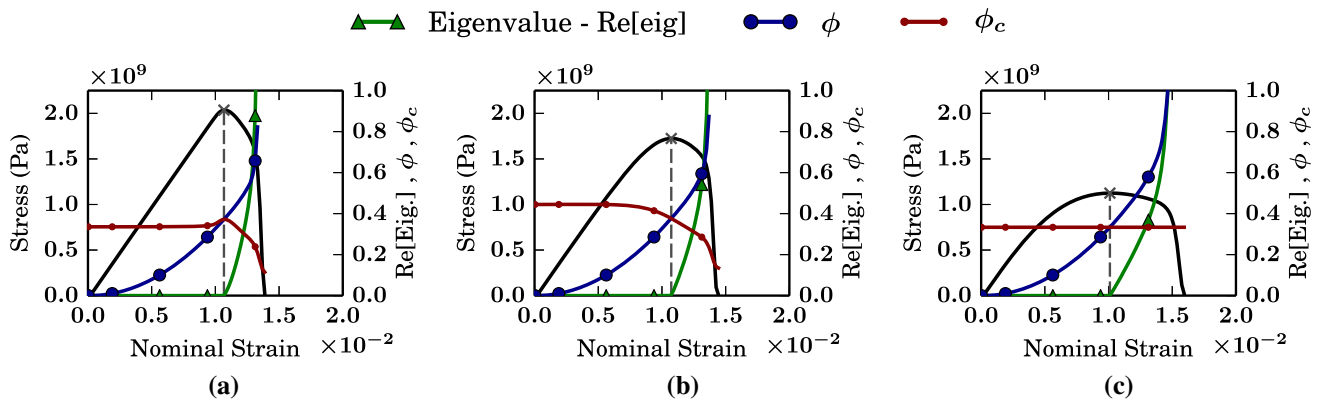


Fig. 11 Comparison between analytical criterion and eigenvalue criterion in an elastic material for different values of the degradation function parameter s **a** $s = 0.01$ **b** $s = 0.5$ **c** $s = 2.0$

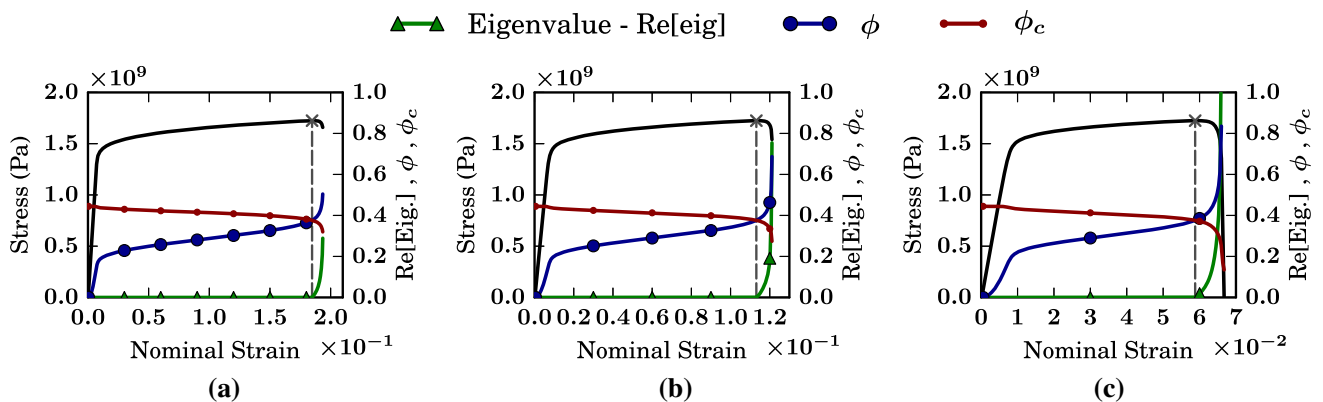


Fig. 12 Comparison between analytical criterion and eigenvalue criterion in an visco-plastic material for different strain-rates and $P^+ = 0$ **a** $\dot{\epsilon} = 1 \times 10^{-3} \text{s}^{-1}$ **b** $\dot{\epsilon} = 2 \times 10^{-3} \text{s}^{-1}$ **c** $\dot{\epsilon} = 5 \times 10^{-3} \text{s}^{-1}$

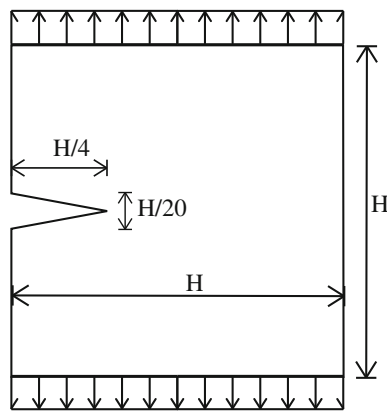


Fig. 13 Full geometry of the square with preexisting crack problem. Dimension $H=10\text{ mm}$

of the nominal strain in Fig. 7a. As the value of s decreases towards the limit value of zero, then c will depart later from the undamaged case ($c = 0$).

Remarkably, all three functions intercept at $c = 1/3$. To understand this we first note that the models are still homogeneous at this point, even though we are already past the instability point. Consequently, the homogeneous solution can be obtained by plugging $\frac{\partial m}{\partial c}$ for the cubic formulation in (4) (note that in elasticity $P^+ = 0$) and is given by

$$\phi = \frac{2c}{3(1-c) [2c + s(\frac{1}{3} - c)]} \tag{47}$$

which means that if $c = 1/3$, then the value of the nominal strain for the homogeneous solution is independent of s , causing the intersection. This expression also recovers the critical value of $c = 1/4$ for the elastic case ($s = 2$) as shown in the literature [15,25].

Figure 7b depicts the value of the degradation function with respect to the nominal strain. The advantage of the cubic degradation function is demonstrated as it prevents

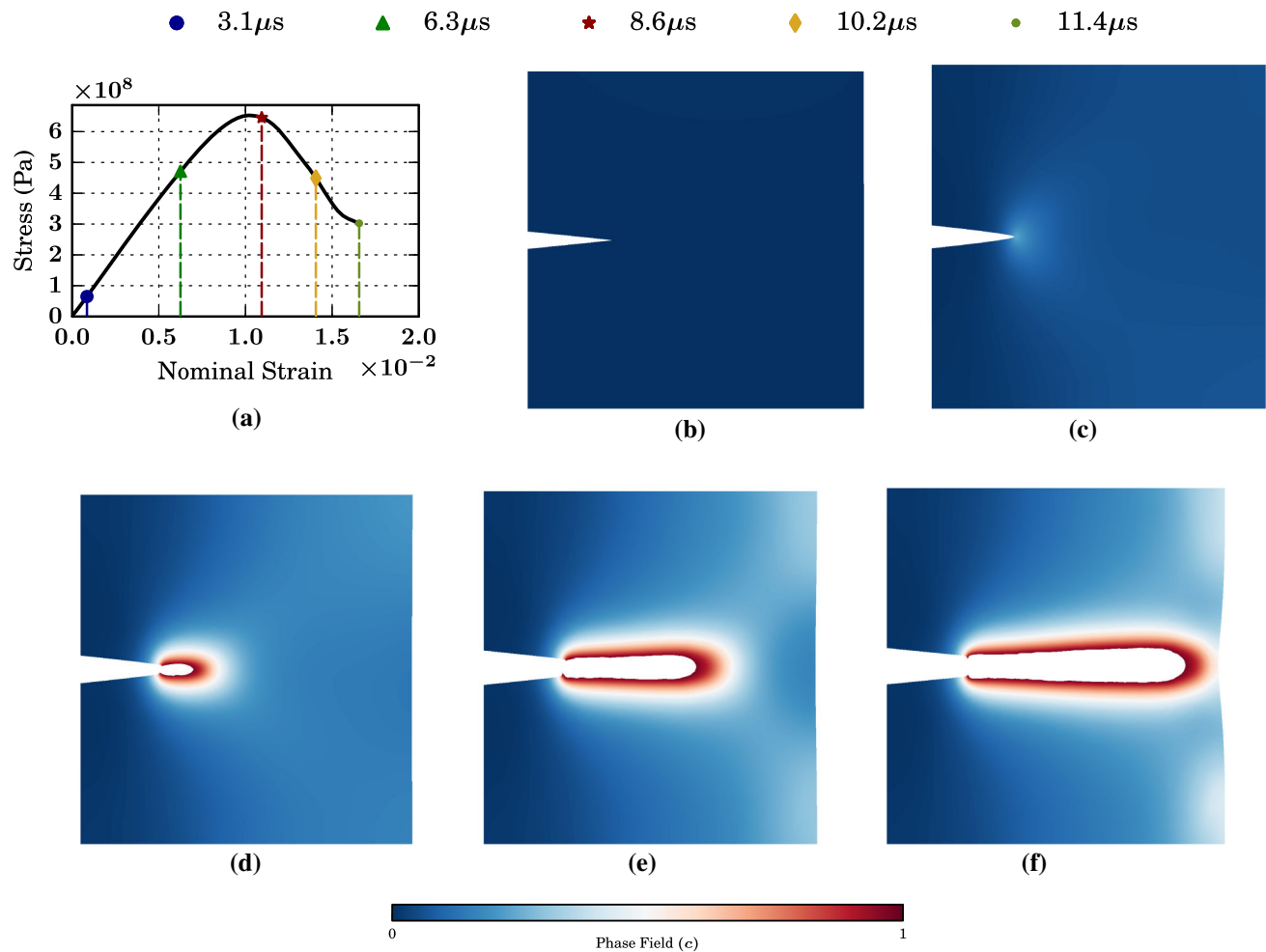


Fig. 14 Snapshots of the phase field parameter distribution in the plate at different times. The results shown here correspond to the elastic model. The mesh is deformed according to the displacement field and

fracture develops in Mode I at the middle of the plate **a** stress versus strain **b** $t=3.1 \mu\text{s}$ **c** $t=6.3 \mu\text{s}$ **d** $t=8.6 \mu\text{s}$ **e** $t=10.2 \mu\text{s}$ **f** $t=11.4 \mu\text{s}$

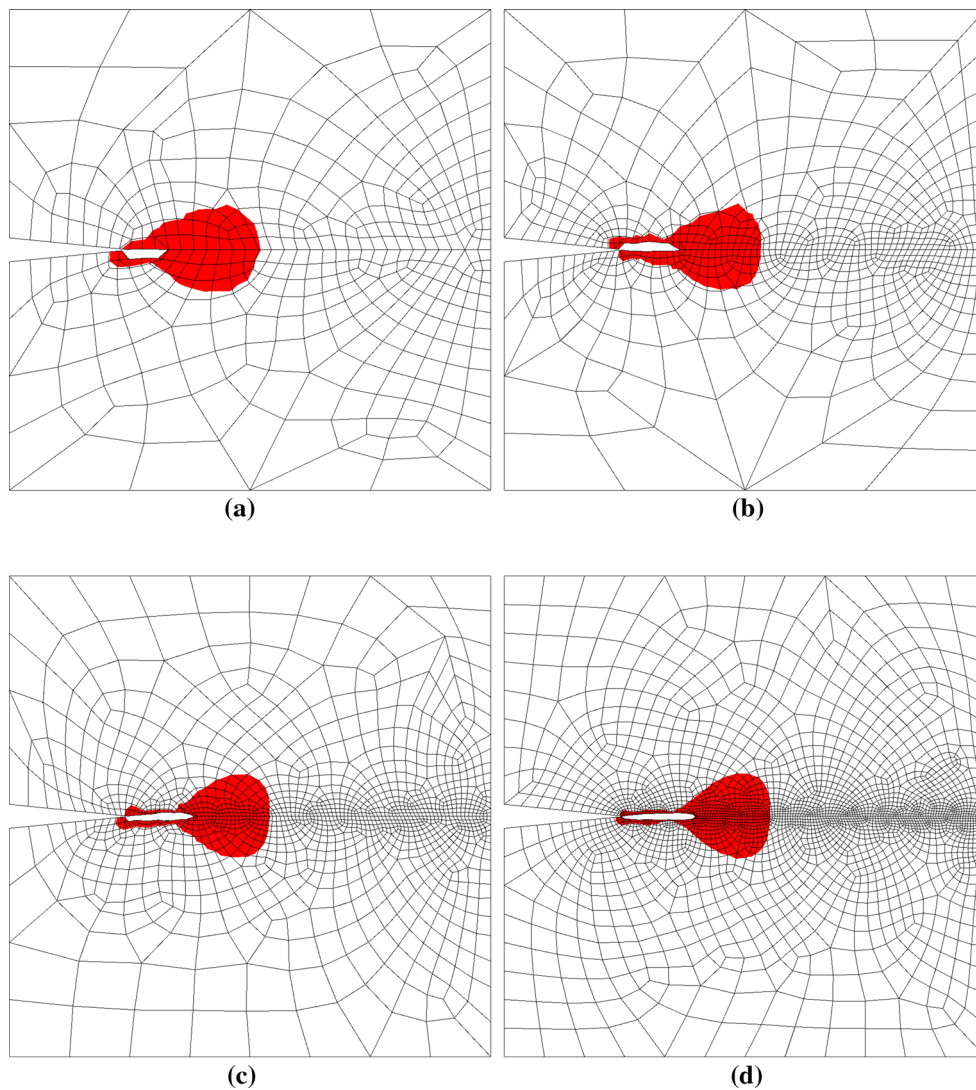


Fig. 15 Stability condition $\phi - \phi_c$ in elastic material with $l_0 = 0.2$ mm at $t = 9 \mu\text{s}$. The *red region* corresponds to a positive criterion and consequently an unstable region. Different mesh sizes are shown to produce

the same unstable region ahead of the crack. Elements belonging to the crack (i.e. $c \geq 0.97$) were removed **a** very coarse mesh **b** coarse mesh **c** medium mesh **d** fine mesh

the material from deteriorating almost up to the critical point (peak stress), allowing for a linear elastic behavior before the onset of degradation. This is in stark contrast to the quadratic formulation that begins degrading from the onset of elastic deformation, driving the material to never exhibit a linear-elastic behavior.

Finally, we show the effect of strain-rate loading in the elastic case. Figure 8 shows the stress-strain curves for both the quadratic case and the cubic case. As expected, the deformation up to the critical point is independent of the strain-rate. However, post instability, the collapse becomes a function of strain-rate, being delayed for increasing strain-rate. This happens because faster rates require larger growth-rates of the perturbation to collapse, which then leads to a delayed collapse.

4.2 Application to a visco-plastic problem

In Figure 9 the stability condition (30) for $s = 0.5$ and different values of strain-rates is plotted for a visco-plastic material with and without the influence of P^+ . As in the elastic material case, the stability condition accurately recovers the peak stress, which confirms the analytical result. The plots corresponding to $P^+ = 0$ have larger values of the critical strain (i.e. the strain at the instability point) when compared to $P^+ \neq 0$. Additionally, the critical stress (i.e. the stress at the instability point) is constant when $P^+ = 0$ but becomes smaller with the decrease in strain-rate for $P^+ \neq 0$. This is due to the fact the lower strain-rates have lower values of the yield stress, which generates more yielding and therefore a stronger contribution of P^+ into the phase-field equation.

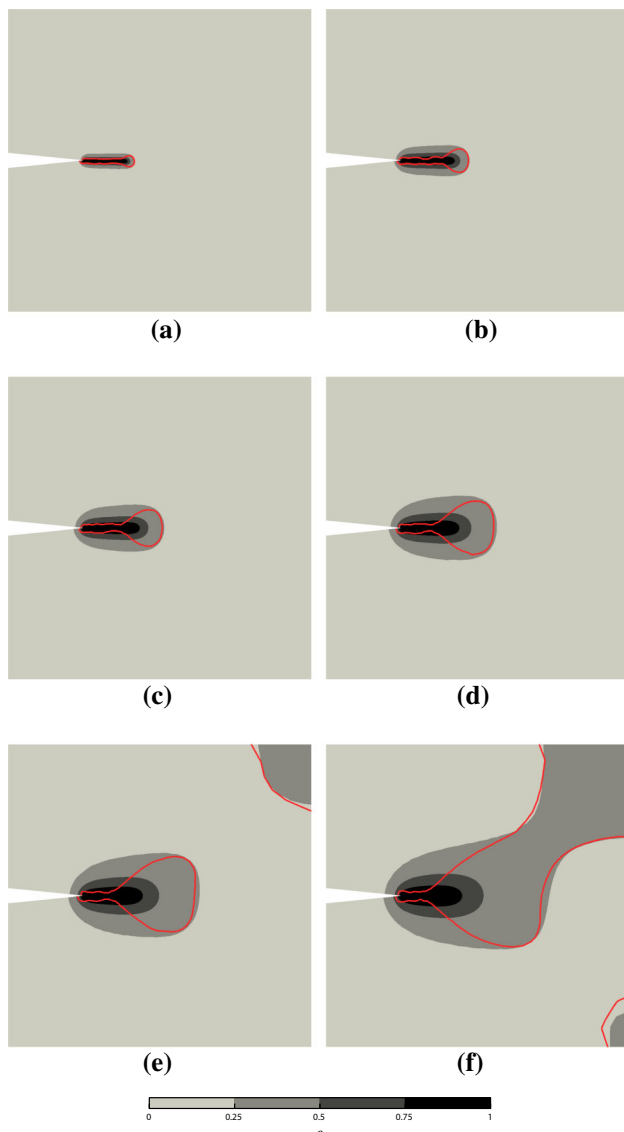


Fig. 16 Influence of the characteristic length l_0 on the size of the unstable region ahead of the crack in an elastic material. The plate is colored based on the value of the phase-field parameter (c) and the condition $\phi = \phi_c$ is delineated with a red line. **a** $l_0 = 0.5\%H$ **b** $l_0 = 1.0\%H$ **c** $l_0 = 1.5\%H$ **d** $l_0 = 2.0\%H$ **e** $l_0 = 2.5\%H$ **f** $l_0 = 3.0\%H$

The critical value of the phase-field parameter (c_c) for the case of $P^+ = 0$ can be computed using Eq. C.1 with the value of s used in this section ($s = 0.5$). Since the value of c_c is a function of only s and f^P , and considering that for $P^+ = 0$ the value of $f^P = 0$, then the critical value of the phase-field parameter is obtained as $c_c = 0.21661$. This can be observed in Fig. 10a, where the crosses were placed based on the condition of $\phi = \phi_c$. On the other hand, if $P^+ \neq 0$, then there is no unique value of the critical c for all strain-rates due to the dependency on f^P . This can be seen in Fig. 10b, where the crosses that represent the critical point given by $\phi = \phi_c$ no longer match a constant value of $c_c = 0.21661$.

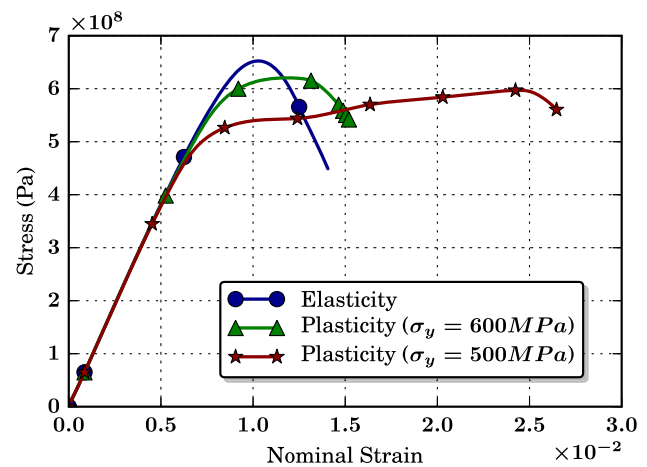


Fig. 17 Stress-strain curves for different values of yield stress. The stress represented here is the average in the entire plate of the Von-mises stress

4.3 Prediction based on numerical eigenvalues construction

In this section we demonstrate that the numerical eigenvalue criterion, i.e. the result of an eigenvalue analysis on the stiffness part of the Jacobian matrix, recovers the analytical result. Figure 11 shows the values of ϕ , ϕ_c and the Eigenvalue as a function of the nominal strain for an elastic material with different values of s .

Figure 12 depicts the same quantities but in a visco-plastic material for different strain-rates. In all cases the the criterion $\phi \geq \phi_c$ is matched by an eigenvalue ω such that $\text{Re}[\omega] \geq 0$.

5 Numerical results in 2D

5.1 A square steel plate with preexisting crack

In this section we study the effect of mesh size and characteristic length (l_0) on the size of the instability region ahead of the crack.

A steel square plate is considered as shown in Fig. 13 with dimension $H = 10$ mm. The plate is stretched uniaxially under a displacement control loading defined by the velocity profile shown in Fig. 32 with $v_r = 10$ m/s, which corresponds to a nominal strain-rate of 10^3 s^{-1} and $t_r = 1.25 \mu\text{s}$. A Johnson–Cook material law is used and the respective parameters are the same as the ones presented in Sect. 2 and Appendix B. Additionally, we also study an elastic material, with a quadratic degradation function and with $l_0 = 0.2$ mm.

In Fig. 14 are depicted several snapshots of the evolution of the crack along time in an elastic material. The crack nucleates at the tip of the preexisting crack and proceeds in mode I along the horizontal direction of the plate. Henceforth the

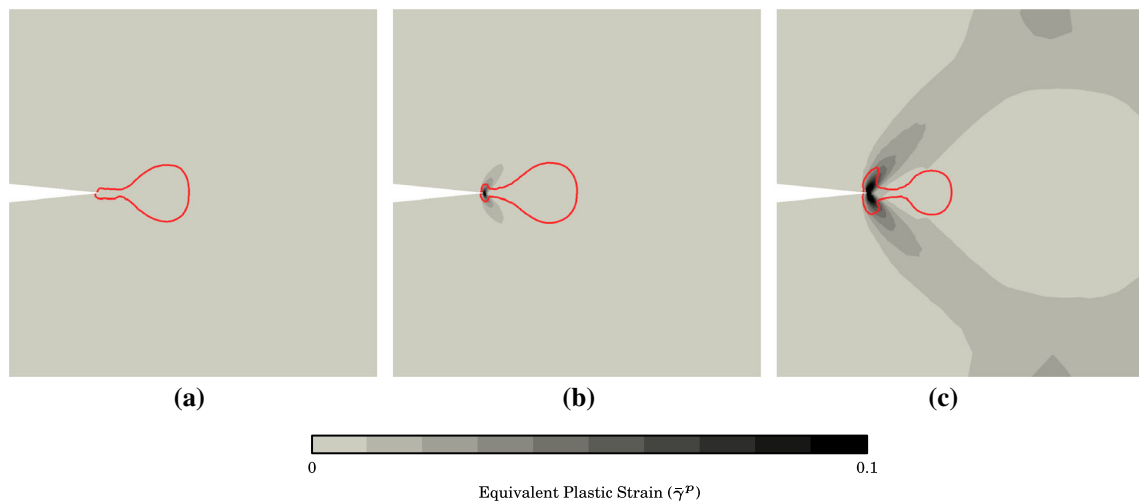


Fig. 18 Influence of the yield stress on the unstable region ahead of the crack. The plate is colored based on the value of the equivalent plastic strain ($\bar{\gamma}^P$) and the condition $\phi = \phi_c$ is delineated with a red line **a** elasticity **b** plasticity - $\sigma_y = 600$ MPa **c** plasticity - $\sigma_y = 500$ MPa

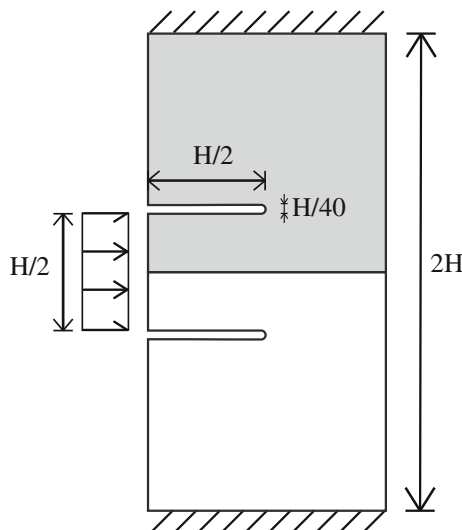


Fig. 19 Full geometry of the notched steel plate problem. Dimension $H = 10$ mm

analysis will focus on the influence of several characteristics of the model in the behavior of the stability condition. Unless otherwise specified, the figures are shown at time $t = 8.6 \mu\text{s}$.

5.1.1 Mesh size

In Fig. 15 we show the effect of mesh size on the stability criterion. The results presented for an elastic material law indicate that the size of the instability region is seemingly unaffected by the mesh density.

Since mesh refinement is in general needed for more accurate crack propagation, this results is particularly important since it suggests that a coarse mesh is sufficient to determine, with reasonable accuracy, the unstable region ahead of

the crack. Consequently, the unstable region may be refined in places where crack propagation is expected to properly capture the steep gradients. Such local refinement allows for good accuracy at a minimal computational cost.

In summary, this result suggests that an efficient and accurate condition for mesh refinement can be based on the stability criterion proposed.

5.1.2 Length scale

The influence of changing the length-scale parameter (l_0) on the size of the unstable region is studied. The length-scale l_0 is taken between 0.5% to 3% of the H dimension of the plate. Figure 16 demonstrates that, as expected, the size of the unstable region ahead of the crack will be related to the value of the phase-field parameter (c), which in turn is strongly affected by the length-scale parameter.

Additionally, notice that the boundary of the unstable region is closely related to the condition $c = 0.25$ which is in accordance with the critical value of the phase-field parameter derived for a 1D homogeneous elastic case by [15] and also shown in Eq. 47.

As expected from the phase-field formulation, if the mesh is sufficiently dense, then a smaller value of l_0 will lead to a sharper and more narrow crack geometry. This is also true for the stability condition, where a smaller value of l_0 leads to a sharper instability region ahead of the crack.

5.1.3 Plasticity and yield stress

The contribution of plasticity and the value of the yield stress has a direct effect on the crack behavior of this problem. In Fig. 17 the average Von-mises stress in the plate as the analysis progresses for different levels of yield stress is shown.

The effect of plasticity is clearly visible in the delay of the crack formation and reduction of the stress.

Figure 18 shows the effect of plasticity and P^+ in the distribution of the unstable points on the domain, i.e. the location of the instability.

The three plots do not correspond to the same point in time but to similar positions of the crack tip during propagation since, as can be seen in Fig. 17, the stress decrease associated with the propagation of fracture is delayed in the presence of plasticity.

Figure 18 reveals that accumulation of plastic deformation near the tip of the initial crack increases the size of the unstable region. This is due to the fact that the material possesses considerable strain hardening, which means that the elastic strains, and consequently the elastic energy, will increase as the regions with larger plastic deformation are subject to more hardening. In fact, the enlarged instability region at the

concentration of plastic deformation remains the same once the crack starts propagating.

5.2 Impact into a notched steel plate—the influence of the type of degradation function

The behavior of a notched steel problem is studied in this section where elasticity is considered and the parameters of the model are given in Section 2 and Appendix B. The geometry of the problem is related to the well known Kalthoff problem[71] and is depicted in Fig. 19. The plate is loaded with displacement control defined by the velocity profile shown in Fig. 32 with $v_r = 10$ m/s, which corresponds to a nominal strain-rate of 10^3 s $^{-1}$ and $t_r = 1.25$ μ s.

Figure 20 depicts the value of the phase-field parameter (c) for an elastic material with a quadratic degradation function ($s = 2$) at different moments in time. The speed of prop-

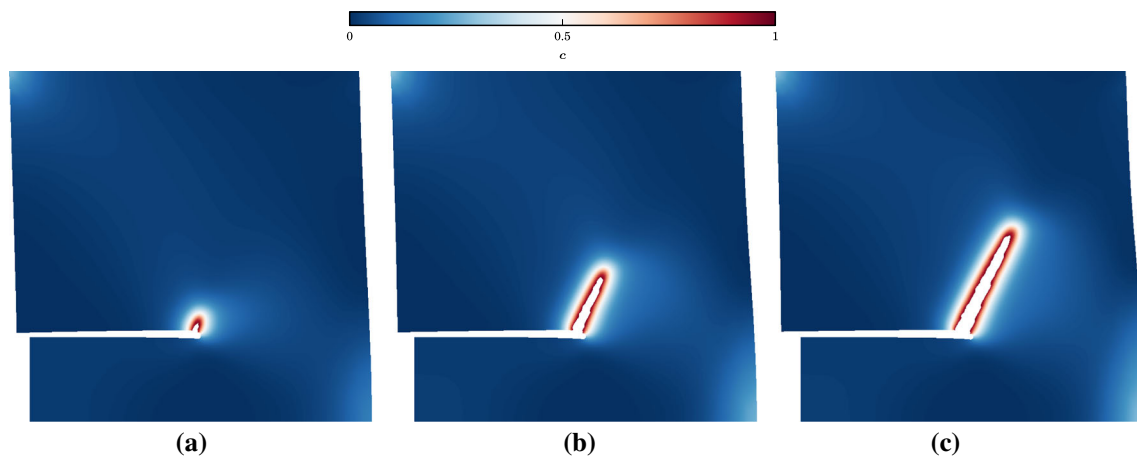


Fig. 20 Evolution of the phase-field parameter in time, showing the propagation of the crack at an angle $\approx 65^\circ$. The material is elastic and a quadratic degradation function is used **a** $t = 16.75$ μ s **b** $t = 18.5$ μ s **c** $t = 19.5$ μ s

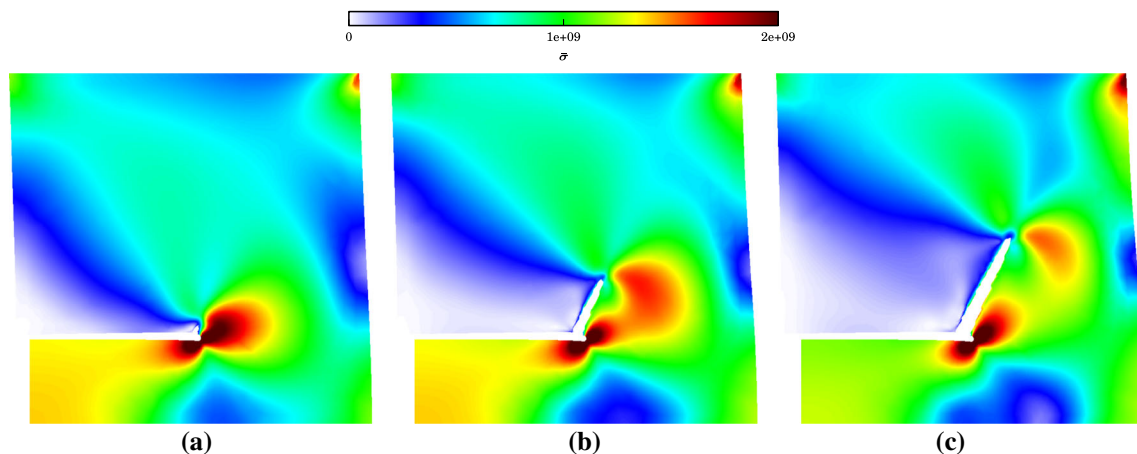
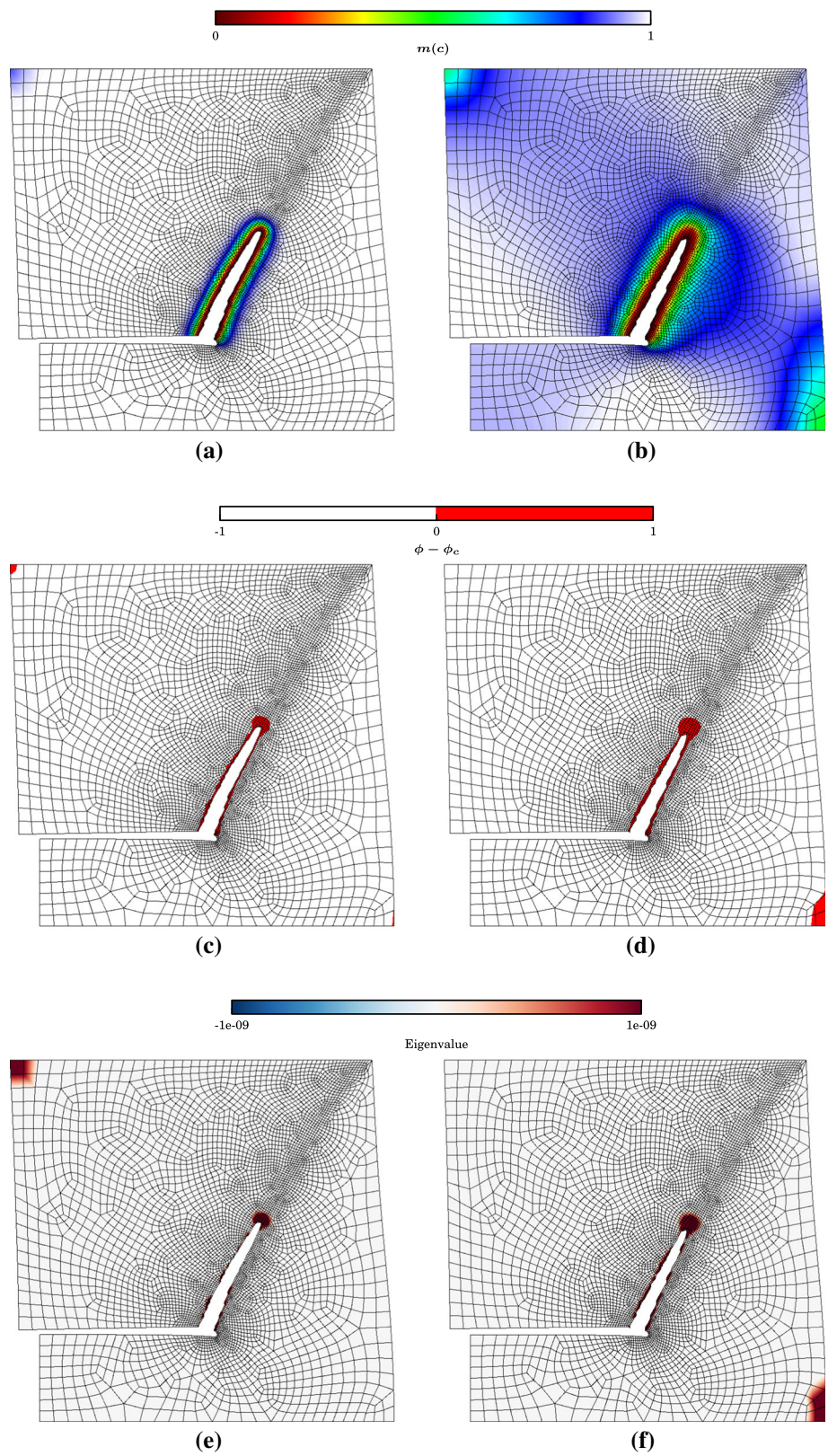


Fig. 21 Evolution of the Von-Mises stress in time, showing the propagation of the crack and the consequent unloading of the solid in the shadow of the crack. The material is elastic and a quadratic

degradation function is used **a** $t = 16.75$ μ s **b** $t = 18.5$ μ s **c** $t = 19.5$ μ s

Fig. 22 Degradation function $m(c)$, Stability condition $\phi - \phi_c$ and eigenvalue condition in elastic material for $t = 20 \mu\text{s}$. **a** and **b** show the degradation function for $s = 0.01$ and $s = 2$, respectively. **c** and **d** show the stability condition for $s = 0.01$ and $s = 2$, respectively. **e** and **f** show the eigenvalue condition for $s = 0.01$ and $s = 2$, respectively



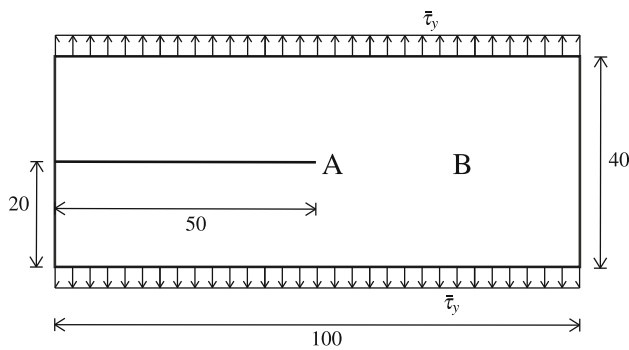


Fig. 23 Full geometry of the branching problem. Dimensions in mm. $\bar{\tau}_y$ is the applied traction at the top and bottom boundary. A and B are two points used for field plots. The point A corresponds to the notch tip and the point B to an intermediate position along the expected crack path

agation and the angle of the crack are in good agreement with the values reported in past literature[71,72]. In Fig. 21 is depicted the evolution of the von-Mises stress in the plate,

showing the stress concentration and the unloading due to the crack.

Figure 22 depicts the value of the degradation function ($m(c)$) and the stability criterion ($\phi - \phi_c$) for a quadratic ($s = 2$) and cubic ($s = 0.01$) behavior of $m(c)$. As expected, the quadratic degradation function tends to degrade more the material away from the crack surface. The stability condition successfully detects the unstable region ahead of the crack for both cases.

5.3 Crack branching benchmark example

Next, we study the behavior of the analytical criterion and the eigenvalue methodology on a crack branching problem. We study a pre-cracked steel plate pulled in Mode I with a constant tension at the boundary. The specifications of the problem are obtained from the literature [15] and reproduced in Fig. 23. The results match previous numerical simulations

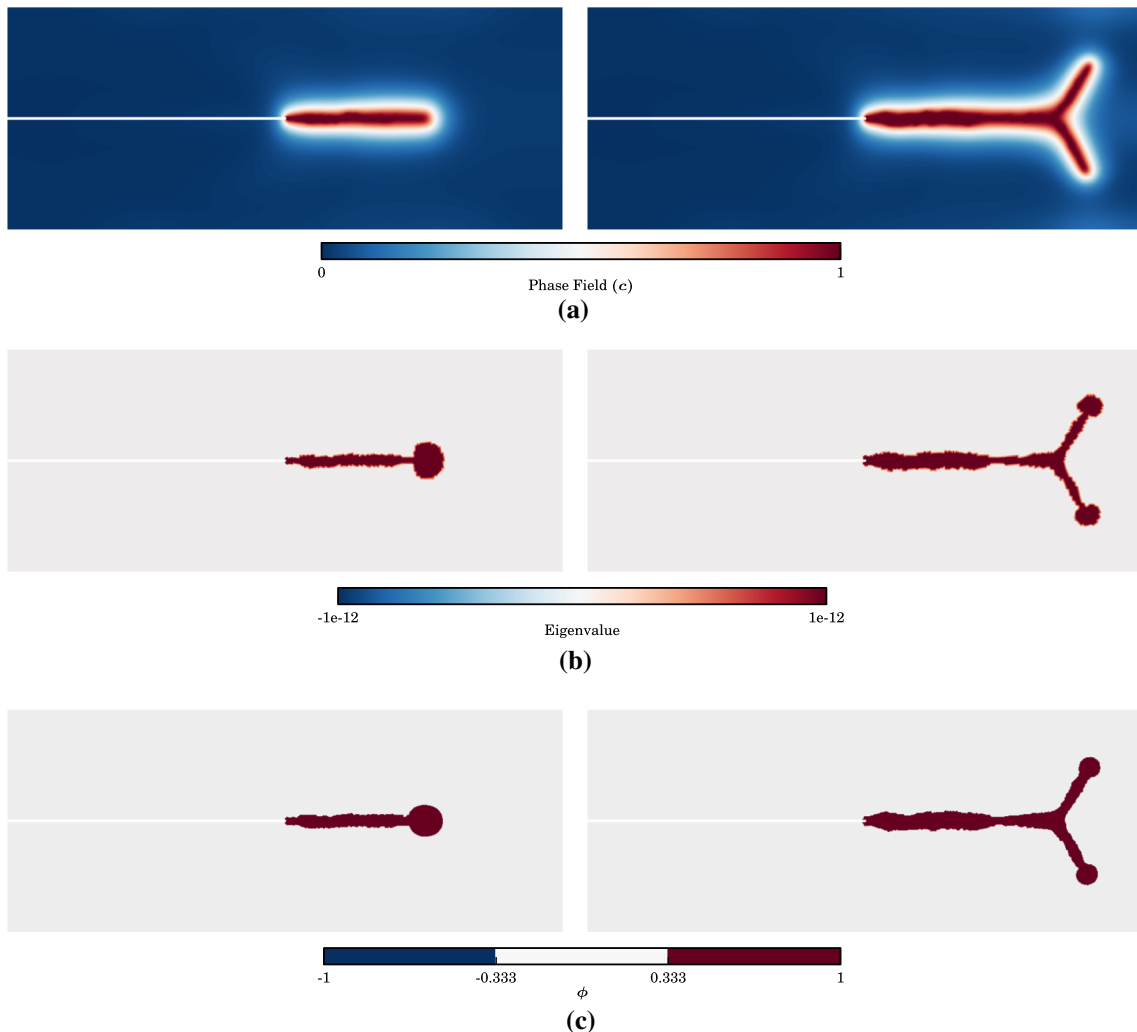


Fig. 24 Crack branching results in an elastic material with quadratic degradation. A comparison between the phase field parameter, the eigenvalues and the ϕ parameter **a** phase field **b** eigenvalue **c** ϕ

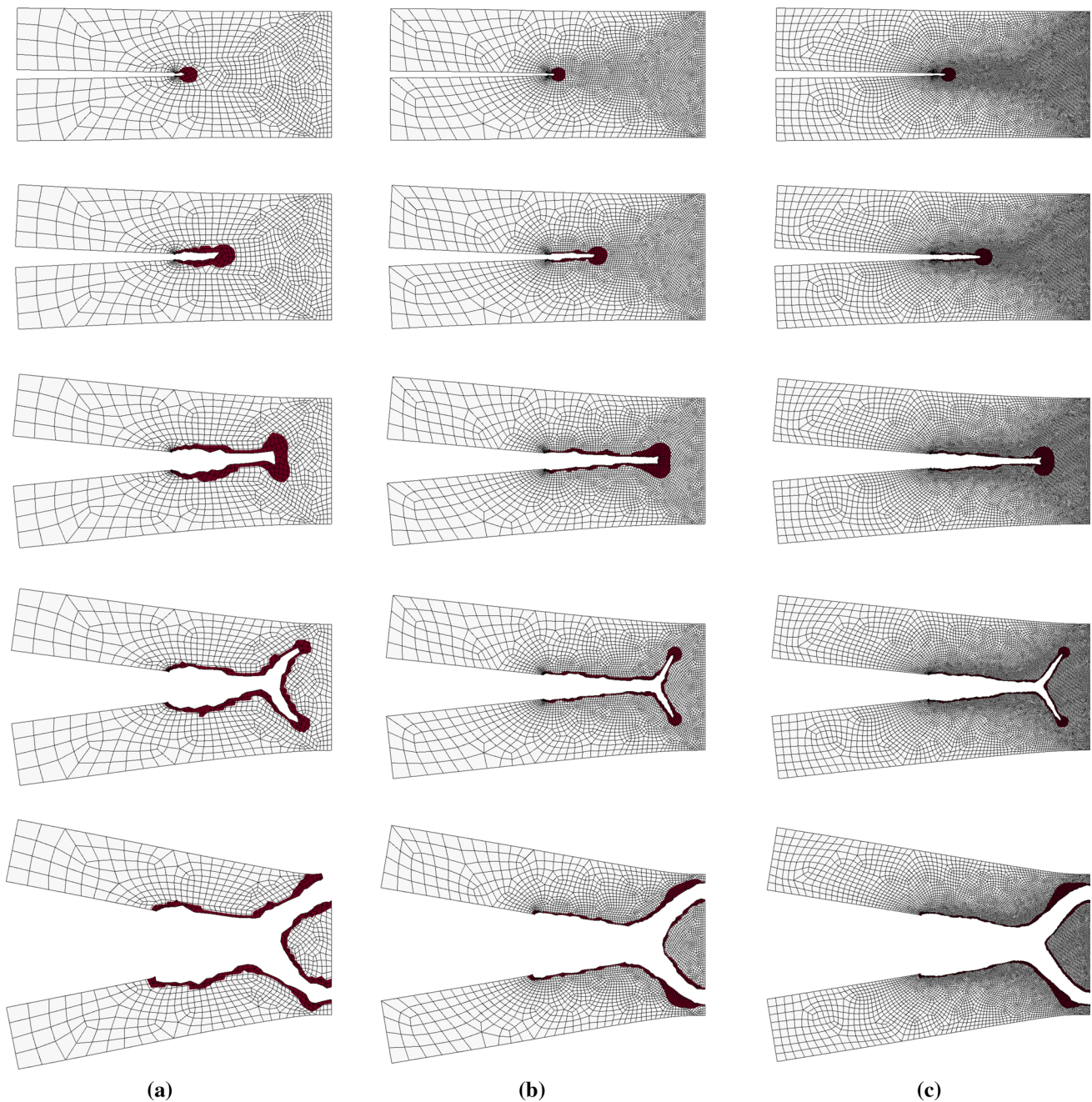


Fig. 25 Snapshots of crack branching results in an elastic material with varying mesh densities. The red shading marks the regions where $\phi > \phi_c = 1/3$. The mesh is deformed proportionally to the displace-

ment field, amplified by a factor of 5. Elements with a phase field value above 0.97 are removed **a** coarse mesh (1062 elements) **b** intermediate mesh (3541 elements) **c** fine mesh (11053 elements)

of the problem using different methods like phase-field[15], XFEM [73] or peridynamics [74], as well as experimental results [75]. A Johnson–Cook material law is used and the respective parameters are the same as the ones presented in Sect. 2 and Appendix B.

The branching problem is modeled assuming an elastic material and a quadratic degradation function.

In Fig. 24 a comparison between the phase field parameter, the eigenvalues and the ϕ parameter for two different moments in time are shown. These results confirm that the condition $\phi > \phi_c$ (where $\phi_c = 1/3$ in a quadratic degradation) predicts well the unstable elements both qualitatively by marking the cracked elements and the crack front, and quantitatively by comparison with

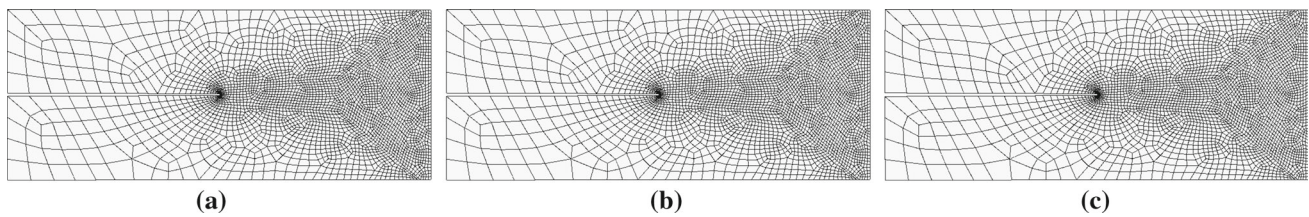


Fig. 26 Crack branching for a very low traction of $\bar{\tau} = 0.1\bar{\tau}_{ref}$. The plotting properties are the same as in Fig. 25. The three snapshots are demarcated in Fig. 30a **a** $t=250\mu s$ **b** $t=500\mu s$ **c** $t=750\mu s$

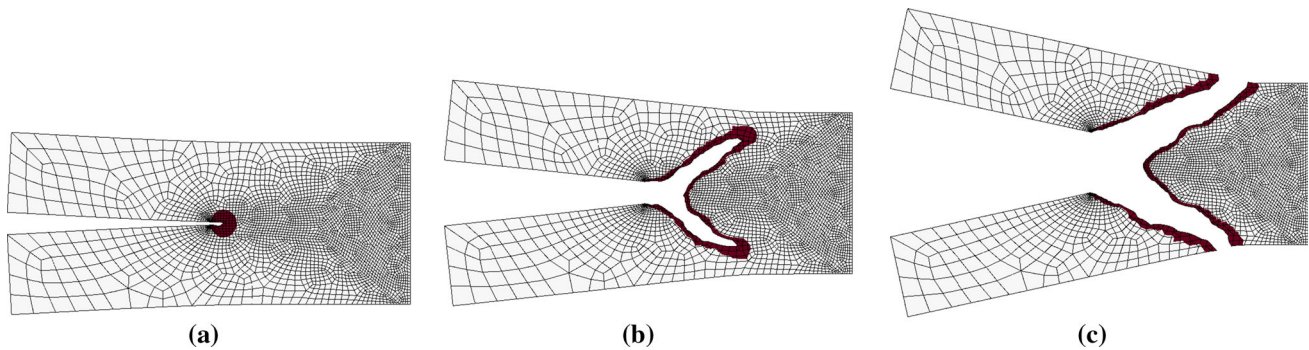


Fig. 27 Crack branching for a low traction of $\bar{\tau} = 0.5\bar{\tau}_{ref}$. The plotting properties are the same as in Fig. 25. The three snapshots are demarcated in Fig. 30b **a** $t=50\mu s$ **b** $t=100\mu s$ **c** $t=150\mu s$

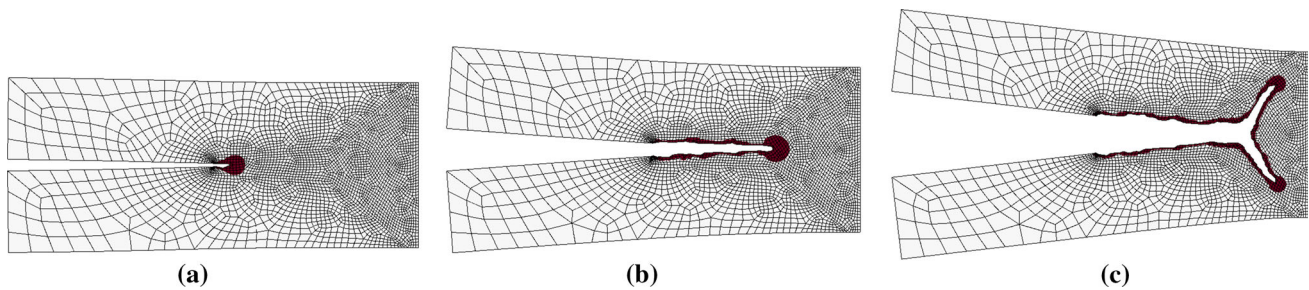


Fig. 28 Crack branching for the reference traction, $\bar{\tau} = 1.0\bar{\tau}_{ref}$. The plotting properties are the same as in Fig. 25. The three snapshots are demarcated in Fig. 30c **a** $t=25\mu s$ **b** $t=50\mu s$ **c** $t=75\mu s$

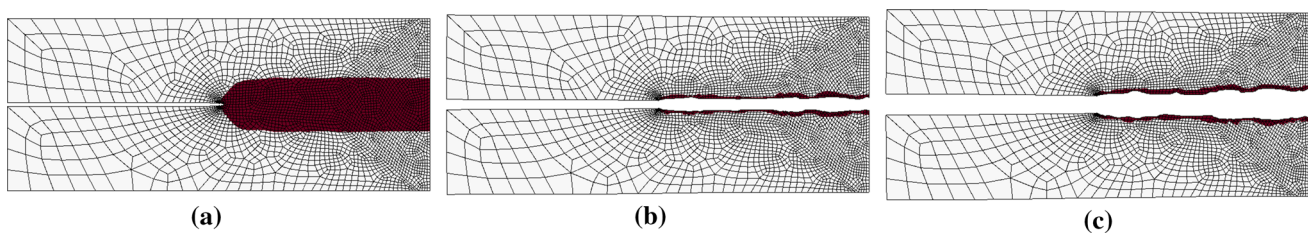


Fig. 29 Crack branching for a high traction of $\bar{\tau} = 4.0\bar{\tau}_{ref}$. The plotting properties are the same as in Fig. 25. The three snapshots are demarcated in Fig. 30d **a** $t=6.25\mu s$ **b** $t=12.5\mu s$ **c** $t=18.75\mu s$

the numerical approach for local instability given by the eigenvalues.

In Fig. 25 the evolution of the problem for three meshes is presented. The value of ϕ is computed for each element and is shown to predict quite accurately the region ahead of the crack where it is about to propagate, including the branching point.

Additionally, notice that the size of the unstable region ahead of the crack seems to be independent of the mesh-size. This confirms the prediction that the intrinsic wave-length that depends on the element size is in fact not restrictive for this problem since the first detection of instability is associated with the uniform mode.

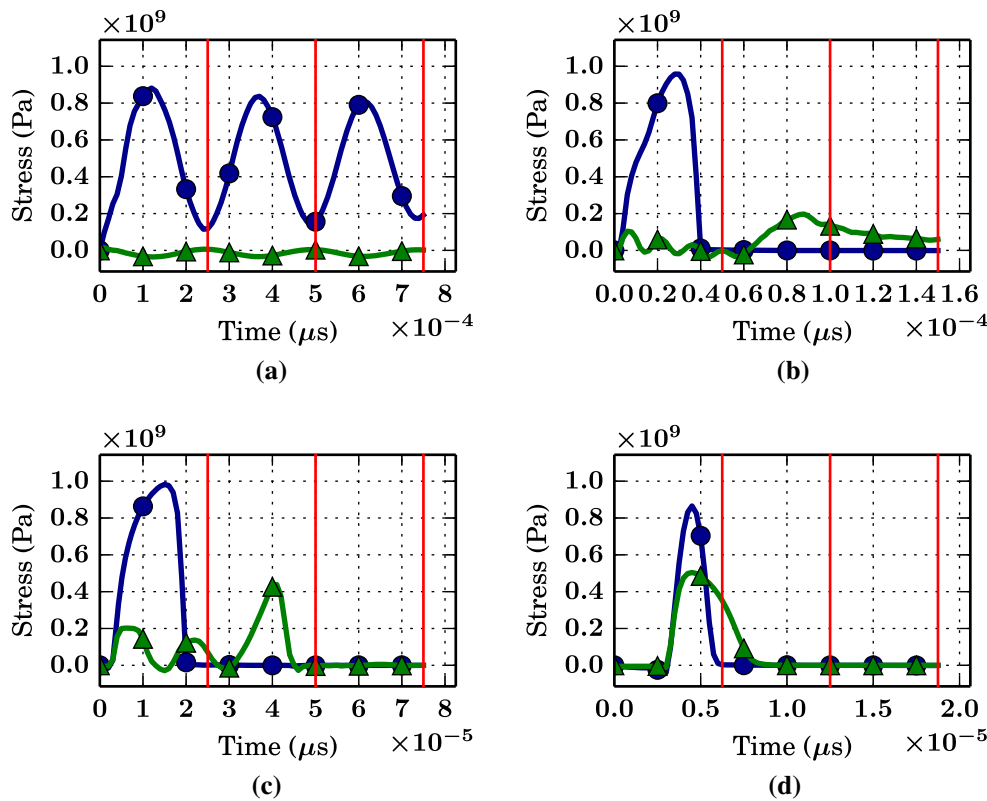


Fig. 30 Stress (σ_{yy}) as a function of time for points A (blue circle) and B (green triangle), corresponding respectively to the points in Fig. 23. The red vertical lines demarcate the three snapshots of the previous figures. Each subfigure is shown with respect to the four dif-

ferent values of applied traction corresponding to Figs. 26–29 **a** very low traction: $\bar{\tau} = 0.1\bar{\tau}_{ref}$. **b** Low traction: $\bar{\tau} = 0.5\bar{\tau}_{ref}$. **c** Reference traction: $\bar{\tau} = 1.0\bar{\tau}_{ref}$. **d** High traction: $\bar{\tau} = 4.0\bar{\tau}_{ref}$

Next we analyze the effect of different traction levels applied to the plate boundaries. Figures 26–29 show the stability condition and crack propagation for four different values of applied traction at the boundary. These traction values are taken as a fraction of the reference traction $\bar{\tau}_{ref}$ used before and are named as very low stress (0.1), low stress (0.5), reference stress (1.0) and high stress (4.0). Each figure shows three snapshots in time. It can be seen in Fig. 26 that the very low traction can only initiate some damage at the crack tip but the loading is not sufficient to cause crack propagation. The low and reference traction levels in Figs. 26–27, respectively, illustrate crack propagation and branching, however, it is interesting to note that the branching point is sensitive to the applied traction and a lower traction level yields earlier branching while the higher (reference) traction results in a later branching. Furthermore, Fig. 29 shows that for very high traction levels, branching does not occur. In this case, the elastic waves due to the loading travel parallel to the boundary and once they meet in the center the crack propagates in a mode I like behavior.

These observations are accompanied by local field plots at point A and B depicted in Fig. 23. Thus, Fig. 30 shows the stress (σ_{yy}) at points A and B as a function of time, for each applied traction. It is interesting to note that in the low traction case in Fig. 30a the stress at point A is strongly oscillating due to dynamic wave propagation and the damage that initiated at this point, while point B is undamaged and only minor dynamic oscillations are observed. Figures 30b, c which correspond to the two branching scenarios illustrated in Figs. 27–28 show that the stress at point A initially increases due to damage accumulation but once damage reaches its peak value the stress collapses and crack propagates through this point. The stress behavior at point B is also initially oscillatory with a rapid increase at some point due to more complex branching effects that occur earlier in the low traction level as compared with the reference traction. Finally, Fig. 30d shows that the stress at points A and B grows at a similar rate which indicates that damage initiates at approximately the same time but then the stress quickly collapses at point A while a more slow collapse is observed at point B due to the effect of the notch tip.

6 Concluding remarks

In this paper, fracture is modeled by the phase-field method and a stability criterion is derived for a general degradation function in visco-plastic materials. The numerical results show good agreement with the theoretical predictions, including the critical value for the phase-field parameter.

It is shown that this condition can be expanded and applied to multi-dimensions. To this end, a series of examples in 2D is investigated and the stability condition successfully detects and predicts the formation and propagation of cracks, even in complex situations like crack branching.

The results are compared to the numerical stability condition given by the eigenvalues of the stiffness part of the element Jacobian matrix. Both approaches show excellent agreement in predicting the instability point, which also serves as a reliability confirmation of the analytical criterion.

Furthermore, the instability region ahead of the crack is shown to be mesh independent and a function of the length-scale parameter l_0 , which is consistent with the phase-field method. Hence in future work, such criterion could provide a reliable approach for local mesh refinement in the path of cracks.

Acknowledgements The financial support of the U.S Department of Energy office of Science, through the Early Career Research Program, No. DE-SC-0008196, and the Army Research Office, under Grant No. W911NF1310238, is gratefully acknowledged.

Appendix A: Terms of the characteristic equation

The characteristic equation in 1D has the following form.

$$C_0 + C_1\tilde{\omega} + C_2\tilde{\omega}^2 + C_3\tilde{\omega}^3 = 0 \quad (\text{A.1})$$

with the following expressions for the coefficients C_0 , C_1 , C_2 and C_3

$$\begin{aligned} C_0 &= B\alpha k^2 \zeta \\ C_1 &= A\alpha k^2 \zeta \\ C_2 &= B [1 + A\zeta + P^g(1 - \zeta) + P^t(1 - \zeta)] \\ C_3 &= A [1 + P^t(1 - \zeta)] \end{aligned}$$

where

$$\tilde{\omega} = \frac{\omega}{f_e} \quad (\text{A.2})$$

$$f_e = \sqrt{\frac{Em_0}{\alpha\rho}} \quad (\text{A.3})$$

$$\zeta = \frac{\theta - \left[\left(\frac{\partial m_0}{\partial c} \right)^2 / m_0 - \frac{(1+f^p)}{2} \frac{\partial^2 m_0}{\partial c^2} \right] \phi}{\theta + \frac{(1+f^p)}{2} \frac{\partial^2 m_0}{\partial c^2} \phi} \quad (\text{A.4})$$

$$A = \frac{Em_0}{Q_0} = \frac{Em_0}{\frac{\partial \tau}{\partial \gamma^p}} \quad (\text{A.5})$$

$$B = \frac{Em_0}{f_e R_0} = \frac{Em_0}{f_e \frac{\partial \tau}{\partial \gamma^p}} \quad (\text{A.6})$$

$$P^t = Em_0 \frac{\partial P_0^+}{\partial \tau} \bigg/ \frac{\partial W_0^+}{\partial \gamma^e} \quad (\text{A.7})$$

$$P^g = \frac{Em_0}{Q_0} \frac{\partial P_0^+}{\partial \gamma^p} \bigg/ \frac{\partial W_0^+}{\partial \gamma^e} \quad (\text{A.8})$$

where $\tilde{\omega}$ is the normalized growth-rate and f_e is the characteristic frequency, which can be understood as the inverse of the time it takes for an elastic wave to propagate through the characteristic length l_0 . The variable ζ condenses the behavior of the phase-field formulation and depends on the non-dimensional parameters that represent the two main drivers of the phase-field equation: the regularization term (in θ) and the source term (in ϕ). The variable ζ also depends on the choice of degradation function and the influence of P^+ on the system.

Appendix B: 1D Numerical properties

The rod is discretized with varying element size to properly capture the localization. Considering symmetry, the relative position of the elements (p) from the center to one edge (half-rod) can be defined by the following function

$$p(\bar{x}) = \begin{cases} S_0 \bar{x} & \text{for } \bar{x} \leq \beta \\ S_0 \bar{x} + (1 - S_0) \left(\frac{\bar{x} - \beta}{1 - \beta} \right)^P & \text{for } \bar{x} > \beta \end{cases} \quad (\text{B.1})$$

where \bar{x} the relative node number, P is the exponent used for varying the element size, β is the percentage of nodes concentrated at the center of the rod with constant element size and S_0 is the slope for the central elements, defined as:

$$S_0 = \frac{d_e}{L} N \quad (\text{B.2})$$

where L and N are the length and the number of nodes of the half-rod, respectively and d_e defines the constant element size in the center of the rod.

In the following sections, the results are presented for $N = 101$, $\beta = 0.25$, $P = 5$, $\frac{d_e}{L} = 1 \times 10^{-4}$ and $L = 0.5 \times 10^{-3}$ m. All values refer to the half-rod, which means that the final length will be 10^{-3} m. The total number of nodes will be 201 since the central node is repeated. Figure 31a shows the relative position of the nodes in the half-rod as a function

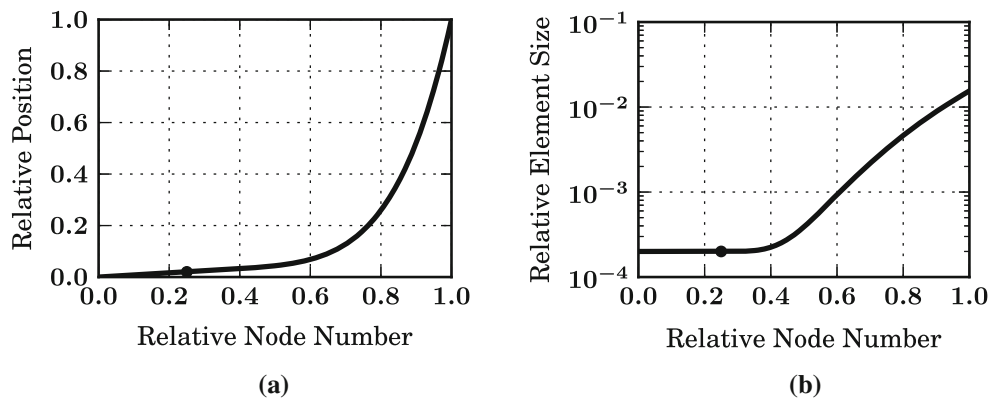


Fig. 31 Representation of a 1D right half-rod. The black dot marks β **a** position of nodes **b** element sizes

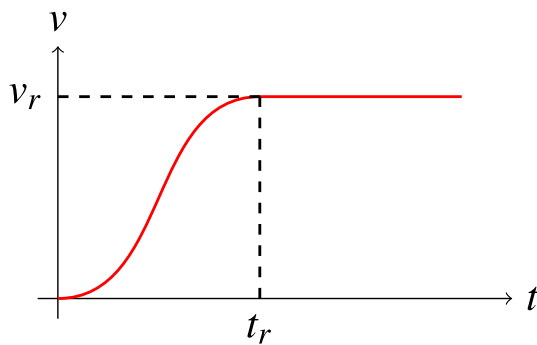


Fig. 32 Velocity profile used as a loading function

of the relative node number and Fig. 31b shows the relative element size also as a function of the relative node number.

A hyperbolic secant type of imperfection is considered at the center of the rod which will scale the material parameters A_s , B_s and G_c by the factor

$$\eta_{imp}(r_n) = 1 - \alpha_{red} \left(\frac{2}{e^{r_n} + e^{-r_n}} \right) \tag{B.3}$$

where α_{red} is the reduction of the material parameters in percentage at the center of the imperfection and r_n is the normalized distance given by

$$r_n(x, y) = \frac{\text{abs}(x - x_0)}{r_0} \tag{B.4}$$

with x_0 representing the center of the imperfection and r_0 its radius. For the problem studied $\alpha_{red} = 0.01$, $r_0 = L/100 \mu\text{m}$ and $x_0 = L/2 = 500 \mu\text{m}$.

The velocity of the loading is defined as shown in Fig. 32 with v_r being the steady velocity and t_r the time to reach that velocity. The S-curve is a polynomial that guarantees that the derivative of the Jerk¹ is continuous. We choose this to avoid

¹ Jerk is the derivative of the Acceleration with respect to time and is the quantity responsible for generating elastic waves.

discontinuities and kinks in the profile of the Jerk since the system is sensitive to the applied velocity.

Appendix C: Critical phase-field c_c

$$c_c = \text{Re} \left[\frac{1}{6a^2(f^p - 5)} \left(-\frac{i(\sqrt{3} - i)K_1}{K_3} + K_2 + i(\sqrt{3} + i)K_3 \right) \right] \tag{C.1}$$

where

$$K_1 = a^2(2a(f^p - 2) + f^p - 3)^2 \tag{C.2}$$

$$K_2 = 2a(a(f^p - 11) + f^p - 7) \tag{C.3}$$

$$K_3 = \sqrt[3]{K_4 + K_5 + \sqrt{-a^6(3a + 2)(f^p - 5)^2(f^p + 1)(K_6 + K_7)}} \tag{C.4}$$

$$K_4 = -8a^6(f^p - 2)^3 - 12a^5(f^p - 3)(f^p - 2)^2 - 3a^4(f^{p3} - 7f^{p2} + 27f^p - 61) \tag{C.5}$$

$$K_5 = a^3(f^{p3} - 9f^{p2} + 3f^p + 77) \tag{C.6}$$

$$K_6 = 16a^3(f^p - 2)^3 + 24a^2(f^p - 3)(f^p - 2)^2 \tag{C.7}$$

$$K_7 = 3a(3f^{p3} - 23f^{p2} + 69f^p - 97) + 8(3f^p - 13) \tag{C.8}$$

with

$$a = \frac{s - 2}{3 - s} \tag{C.9}$$

References

1. Beckermann C, Diepers HJ, Steinbach I, Karma A, Tong X (1999) Modeling melt convection in phase-field simulations of solidification. J Comput Phys 154(2):468–496. doi:10.1006/jcph.1999.6323 ISSN 0021-9991

2. Boettinger WJ, Warren JA, Beckermann C, Karma A (2002) Phase-field simulation of solidification. *Annu Rev Mater Res* 32(1):163–194. doi:[10.1146/annurev.matsci.32.101901.155803](https://doi.org/10.1146/annurev.matsci.32.101901.155803)
3. Jeong J-H, Goldenfeld N, Dantzig JA (2001) Phase field model for three-dimensional dendritic growth with fluid flow. *Phys Rev E* 64(4):041602. doi:[10.1103/PhysRevE.64.041602](https://doi.org/10.1103/PhysRevE.64.041602)
4. Wen Y H, Wang Y, Chen L Q (2000) Phase-field simulation of domain structure evolution during a coherent hexagonal-to-orthorhombic transformation. *Philos Mag A* 80(9):1967–1982 ISSN 0141-8610
5. Zaeem M A, Mesarovic S D (2010) Finite element method for conserved phase fields: stress-mediated diffusional phase transformation. *J Comput Phys* 229(24):9135–9149. doi:[10.1016/j.jcp.2010.08.027](https://doi.org/10.1016/j.jcp.2010.08.027) ISSN 0021-9991
6. Wang Y, Khachaturyan A G (1997) Three-dimensional field model and computer modeling of martensitic transformations. *Acta Mater* 45(2):759–773. doi:[10.1016/S1359-6454\(96\)00180-2](https://doi.org/10.1016/S1359-6454(96)00180-2) ISSN 1359-6454
7. Mamivand M, Zaeem MA, El Kadiri H (2013) A review on phase field modeling of martensitic phase transformation. *Comput Mater Sci* 77:304–311. doi:[10.1016/j.commatsci.2013.04.059](https://doi.org/10.1016/j.commatsci.2013.04.059) ISSN 0927–0256
8. Wang Y U, Jin Y M, Cuitiño A M, Khachaturyan A G (2001) Nanoscale phase field microelasticity theory of dislocations: model and 3D simulations. *Acta Mater* 49(10):1847–1857. doi:[10.1016/S1359-6454\(01\)00075-1](https://doi.org/10.1016/S1359-6454(01)00075-1) ISSN 1359-6454
9. Fan D, Chen L Q (1997) Computer simulation of grain growth using a continuum field model. *Acta Mater* 45(2):611–622. doi:[10.1016/S1359-6454\(96\)00200-5](https://doi.org/10.1016/S1359-6454(96)00200-5) ISSN 1359-6454
10. Kazaryan A, Wang Y, Dregia SA, Patton BR (2000) Generalized phase-field model for computer simulation of grain growth in anisotropic systems. *Phys Rev B* 61(21):14275–14278. doi:[10.1103/PhysRevB.61.14275](https://doi.org/10.1103/PhysRevB.61.14275)
11. Clayton JD, Knap J (2011) A phase field model of deformation twinning: nonlinear theory and numerical simulations. *Phys D Nonlinear Phenom* 240(9–10):841–858. doi:[10.1016/j.physd.2010.12.012](https://doi.org/10.1016/j.physd.2010.12.012)ISSN0167-2789
12. Clayton JD, Knap J (2016) Phase field modeling and simulation of coupled fracture and twinning in single crystals and polycrystals. *Comput Methods Appl Mech Eng*, ISSN 0045-7825. doi:[10.1016/j.cma.2016.01.023](https://doi.org/10.1016/j.cma.2016.01.023)
13. Heo T W, Wang Y, Bhattacharya S, Sun X, Hu S, Chen L-Q (2011) A phase-field model for deformation twinning. *Philos Mag Lett* 91(2):110–121. doi:[10.1080/09500839.2010.537284](https://doi.org/10.1080/09500839.2010.537284) ISSN 0950-0839
14. Amor H, Marigo J-J, Maurini C (2009) Regularized formulation of the variational brittle fracture with unilateral contact: numerical experiments. *J Mech Phys Solids* 57(8):1209–1229. doi:[10.1016/j.jmps.2009.04.011](https://doi.org/10.1016/j.jmps.2009.04.011) ISSN 0022-5096
15. Borden MJ, Verhoosel CV, Scott MA, Hughes TJR, Landis CM (2012) A phase-field description of dynamic brittle fracture. *Comput Methods Appl Mech Eng*, 217–220, 77–95. ISSN 0045–7825. doi:[10.1016/j.cma.2012.01.008](https://doi.org/10.1016/j.cma.2012.01.008)
16. Bourdin B, Francfort G A, Marigo J-J (2000) Numerical experiments in revisited brittle fracture. *J Mech Phys Solids* 48(4):797–826. doi:[10.1016/S0022-5096\(99\)00028-9](https://doi.org/10.1016/S0022-5096(99)00028-9) ISSN 0022-5096
17. Duda FP, Ciaronetti A, Sánchez PJ, Huespe AE (2015) A phase-field/gradient damage model for brittle fracture in elastic-plastic solids. *Int J Plast* 65:269–296. doi:[10.1016/j.ijplas.2014.09.005](https://doi.org/10.1016/j.ijplas.2014.09.005) ISSN 0749–6419
18. Kuhn C, Müller R (2013) Crack nucleation in phase field fracture models, In: ICF13
19. May S, Vignollet J, de Borst R (2015) A numerical assessment of phase-field models for brittle and cohesive fracture: Γ -Convergence and stress oscillations. *Eur J Mech A Solids* 52:72–84. doi:[10.1016/j.euromechsol.2015.02.002](https://doi.org/10.1016/j.euromechsol.2015.02.002) ISSN 0997–7538
20. Miehe C, Hofacker M, Welschinger F (2010) A phase field model for rate-independent crack propagation: robust algorithmic implementation based on operator splits. *Comput Methods Appl Mech Eng* 199(45–48):2765–2778. doi:[10.1016/j.cma.2010.04.011](https://doi.org/10.1016/j.cma.2010.04.011) ISSN 0045-7825
21. Miehe C, Welschinger F, Hofacker M (2010b) Thermodynamically consistent phase-field models of fracture: variational principles and multi-field FE implementations. *Int J Numer Methods Eng* 83(10):1273–1311. doi:[10.1002/nme.2861](https://doi.org/10.1002/nme.2861) ISSN 1097-0207
22. Vignollet J, May S, Borst Rd, Verhoosel CV (2014) Phase-field models for brittle and cohesive fracture. *Meccanica*, 49(11): 2587–2601. ISSN 0025–6455, 1572–9648. doi:[10.1007/s11012-013-9862-0](https://doi.org/10.1007/s11012-013-9862-0)
23. Karma A, Lobkovsky AE (2004) Unsteady crack motion and branching in a phase-field model of brittle fracture. *Phys Rev Lett* 92(24):245510. doi:[10.1103/PhysRevLett.92.245510](https://doi.org/10.1103/PhysRevLett.92.245510)
24. Arriaga M, Waisman H (2017) Combined stability analysis of phase-field dynamic fracture and shear band localization. *Int J Plast*, ISSN 0749-6419. doi:[10.1016/j.ijplas.2017.04.018](https://doi.org/10.1016/j.ijplas.2017.04.018)
25. Clayton JD, Knap J (2015) Nonlinear phase field theory for fracture and twinning with analysis of simple shear. *Philos Mag* 95(24):2661–2696. doi:[10.1080/14786435.2015.1076176](https://doi.org/10.1080/14786435.2015.1076176) ISSN 1478-6435
26. Klinsmann M, Rosato D, Kamlah M, McMeeking RM (2015) An assessment of the phase field formulation for crack growth. *Comput Methods Appl Mech Eng* 294:313–330. doi:[10.1016/j.cma.2015.06.009](https://doi.org/10.1016/j.cma.2015.06.009) ISSN 0045–7825
27. Pham K, Marigo J-J (2011) From the onset of damage to rupture: construction of responses with damage localization for a general class of gradient damage models. *Contin Mech Thermodyn*, 25(2–4): 147–171. ISSN 0935–1175, 1432–0959. doi:[10.1007/s00161-011-0228-3](https://doi.org/10.1007/s00161-011-0228-3)
28. Voyiadjis GZ, Mozaffari N (2013) Nonlocal damage model using the phase field method: theory and applications. *Int J Solids Struct* 50(20–21):3136–3151. doi:[10.1016/j.ijsolstr.2013.05.015](https://doi.org/10.1016/j.ijsolstr.2013.05.015) ISSN 0020-7683
29. de Borst R, Verhoosel CV (2016) Gradient damage vs phase-field approaches for fracture: similarities and differences. *Comput Methods Appl Mech Eng*, ISSN 0045-7825. doi:[10.1016/j.cma.2016.05.015](https://doi.org/10.1016/j.cma.2016.05.015)
30. De Borst R (1988) Bifurcations in finite element models with a non-associated flow law. *Int J Numer Anal Methods Geomech* 12(1):99–116. doi:[10.1002/nag.1610120107](https://doi.org/10.1002/nag.1610120107) ISSN 1096-9853
31. Needleman A (1979) Non-normality and bifurcation in plane strain tension and compression. *J Mech Phys Solids* 27(3):231–254. doi:[10.1016/0022-5096\(79\)90003-6](https://doi.org/10.1016/0022-5096(79)90003-6) ISSN 0022-5096
32. Bigoni D (2000) Bifurcation and instability of non-associative elastoplastic solids. In: Petryk H (ed) *Material instabilities in elastic and plastic solids*. Springer, Berlin, pp 1–52
33. de Borst R (1987) Computation of post-bifurcation and post-failure behavior of strain-softening solids. *Comput Struct* 25(2):211–224. doi:[10.1016/0045-7949\(87\)90144-1](https://doi.org/10.1016/0045-7949(87)90144-1) ISSN 0045-7949
34. Pham K, Amor H, Marigo J-J, Maurini C (2011) Gradient damage models and their use to approximate brittle fracture. *Int J Damage Mech*, 20(4): 618–652. ISSN 1056–7895, 1530–7921. doi:[10.1177/1056789510386852](https://doi.org/10.1177/1056789510386852)
35. Abu Al-Rub RK, Voyiadjis GZ (2006) A finite strain plastic-damage model for high velocity impact using combined viscosity and gradient localization limiters: part I—theoretical formulation. *Int J Damage Mech*, 15(4): 293–334, ISSN 1056–7895, 1530–7921. doi:[10.1177/1056789506058046](https://doi.org/10.1177/1056789506058046)
36. Belytschko T, Chiang H-Y, Plaskacz E (1994) High resolution two-dimensional shear band computations: imperfections and mesh dependence. *Comput Methods Appl Mech Eng* 119(1–2):1–15. doi:[10.1016/0045-7825\(94\)00073-5](https://doi.org/10.1016/0045-7825(94)00073-5) ISSN 0045-7825

37. Wright T, Batra R (1985) The initiation and growth of adiabatic shear bands. *Int J Plast* 1(3):205–212. doi:[10.1016/0749-6419\(85\)90003-8](https://doi.org/10.1016/0749-6419(85)90003-8) ISSN 0749-6419
38. Bai Y (1982) Thermo-plastic instability in simple shear. *J Mech Phys Solids* 30(4):195–207. doi:[10.1016/0022-5096\(82\)90029-1](https://doi.org/10.1016/0022-5096(82)90029-1) ISSN 0022-5096
39. Arriaga M, McAuliffe C, Waisman H (2015) Onset of shear band localization by a local generalized eigenvalue analysis. *Comput Methods Appl Mech Eng* 289:179–208. doi:[10.1016/j.cma.2015.02.010](https://doi.org/10.1016/j.cma.2015.02.010) ISSN 0045–7825
40. Arriaga M, McAuliffe C, Waisman H (2016) Instability analysis of shear bands using the instantaneous growth-rate method. *Int J Impact Eng* 87:156–168. doi:[10.1016/j.ijimpeng.2015.04.004](https://doi.org/10.1016/j.ijimpeng.2015.04.004) ISSN 0734-743X
41. Rabczuk T, Areias PMA, Belytschko T (2007) A simplified mesh-free method for shear bands with cohesive surfaces. *Int J Numer Methods Eng* 69(5):993–1021. doi:[10.1002/nme.1797](https://doi.org/10.1002/nme.1797) ISSN 1097-0207
42. Belytschko T, Chen H, Xu J, Zi G (2003) Dynamic crack propagation based on loss of hyperbolicity and a new discontinuous enrichment. *Int J Numer Methods Eng* 58(12):1873–1905. doi:[10.1002/nme.941](https://doi.org/10.1002/nme.941) ISSN 1097-0207
43. Song J-H, Areias PMA, Belytschko T (2006) A method for dynamic crack and shear band propagation with phantom nodes. *Int Numer Methods Eng* 67(6):868–893. doi:[10.1002/nme.1652](https://doi.org/10.1002/nme.1652) ISSN 1097-0207
44. Belytschko T, Loehnert S, Song J-H (2008) Multiscale aggregating discontinuities: a method for circumventing loss of material stability. *Int J Numer Methods Eng* 73(6):869–894. doi:[10.1002/nme.2156](https://doi.org/10.1002/nme.2156) ISSN 1097-0207
45. Tabarraei A, Song J-H, Waisman H (2013) A two-scale strong discontinuity approach for evolution of shear bands under dynamic impact loads. *Int J Multiscale Comput Eng* 11(6):543–563. doi:[10.1615/IntJMultCompEng.2013005506](https://doi.org/10.1615/IntJMultCompEng.2013005506) ISSN 1543-1649
46. Rabczuk T, Samaniego E (2008) Discontinuous modelling of shear bands using adaptive meshfree methods. *Comput Methods Appl Mech Eng* 197(6–8):641–658. doi:[10.1016/j.cma.2007.08.027](https://doi.org/10.1016/j.cma.2007.08.027) ISSN 0045-7825
47. Kuhn C, Schlüter A, Müller R (2015) On degradation functions in phase field fracture models. *Comput Mater Sci* 108(Part B): 374–384. ISSN 0927–0256. doi:[10.1016/j.commatsci.2015.05.034](https://doi.org/10.1016/j.commatsci.2015.05.034)
48. Borden MJ (2012) Isogeometric analysis of phase-field models for dynamic brittle and ductile fracture, thesis, University of Texas at Austin
49. Arriaga M, Waisman H (2017) Stability analysis of the phase-field method for fracture with a general degradation function and plasticity induced crack generation. *Mech Mater*, ISSN 0167-6636. doi:[10.1016/j.mechmat.2017.04.003](https://doi.org/10.1016/j.mechmat.2017.04.003)
50. Lemonds J, Needleman A (1986) Finite element analyses of shear localization in rate and temperature dependent solids. *Mech Mater* 5(4):339–361. doi:[10.1016/0167-6636\(86\)90039-6](https://doi.org/10.1016/0167-6636(86)90039-6) ISSN 0167-6636
51. Needleman A (1988) Material rate dependence and mesh sensitivity in localization problems. *Comput Methods Appl Mech Eng* 67(1):69–85. doi:[10.1016/0045-7825\(88\)90069-2](https://doi.org/10.1016/0045-7825(88)90069-2) ISSN 0045-7825
52. Anand L, Kim K, Shawki T (1987) Onset of shear localization in viscoplastic solids. *J Mech Phys Solids* 35(4):407–429. doi:[10.1016/0022-5096\(87\)90045-7](https://doi.org/10.1016/0022-5096(87)90045-7) ISSN 0022-5096
53. Batra R, Wei Z (2007) Instability strain and shear band spacing in simple tensile/compressive deformations of thermoviscoplastic materials. *Int Impact Eng* 34(3):448–463. doi:[10.1016/j.ijimpeng.2005.11.004](https://doi.org/10.1016/j.ijimpeng.2005.11.004) ISSN 0734-743X
54. Dai L, Bai Y (2008) Basic mechanical behaviors and mechanics of shear banding in BMGs. *Int J Impact Eng* 35(8):704–716. doi:[10.1016/j.ijimpeng.2007.10.007](https://doi.org/10.1016/j.ijimpeng.2007.10.007) ISSN 0734-743X
55. McAuliffe C, Waisman H (2015) A unified model for metal failure capturing shear banding and fracture. *Int J Plast* 65:131–151. doi:[10.1016/j.ijplas.2014.08.016](https://doi.org/10.1016/j.ijplas.2014.08.016) ISSN 0749–6419
56. Braides A (1998) Approximation of free-discontinuity problems. Springer, Berlin ISBN 978-3-540-64771-3
57. McAuliffe C, Waisman H (2016) A coupled phase field shear band model for ductile-brittle transition in notched plate impacts. *Comput Methods Appl Mech Eng* 305:173–195. doi:[10.1016/j.cma.2016.02.018](https://doi.org/10.1016/j.cma.2016.02.018) ISSN 0045–7825
58. Taylor GI, Quinney H (1934) The latent energy remaining in a metal after cold working. In *Proceedings of the Royal Society of London. Series A* 143(849): 307–326. ISSN 1364-5021, 1471-2946. doi:[10.1098/rspa.1934.0004](https://doi.org/10.1098/rspa.1934.0004)
59. Johnson GR, Cook WH (1985) Fracture characteristics of three metals subjected to various strains, strain rates, temperatures and pressures. *Eng Fract Mech* 21(1):31–48. doi:[10.1016/0013-7944\(85\)90052-9](https://doi.org/10.1016/0013-7944(85)90052-9) ISSN 0013-7944
60. Litonski J (1977) Plastic flow of a tube under adiabatic torsion. *Bull Acad Pol Sci Ser Sci Tech* 25(1):7–14
61. Leroy Y, Ortiz M (1990) Finite element analysis of transient strain localization phenomena in frictional solids. *Int J Numer Anal Methods Geomech* 14(2):93–124. doi:[10.1002/nag.1610140203](https://doi.org/10.1002/nag.1610140203) ISSN 1096-9853
62. Babuška PI (1971) Error-bounds for finite element method. *Numer Math* 16(4):322–333. doi:[10.1007/BF02165003](https://doi.org/10.1007/BF02165003) ISSN 0029-599X
63. Brezzi F (1974) On the existence, uniqueness and approximation of saddle-point problems arising from lagrangian multipliers. *ESAIM: Math Model Numer Anal- Modélisation Mathématique et Analyse Numérique* 8(R2):129–151
64. Reissner E (1950) On a variational theorem in elasticity. *J Math Phys* 29(2):90–95
65. Gâteaux M (1913) Sur les fonctionnelles continues et les fonctionnelles analytiques. *CR Acad Sci Paris* 157:325–327
66. Newmark NM (1959) A method of computation for structural dynamics. *J Eng Mech Div* 85(3):67–94
67. Taylor R L (2014) FEAP—Finite element analysis program
68. Hopkinson B (1914) A method of measuring the pressure produced in the detonation of high explosives or by the impact of bullets. *Philosophical Transactions of the Royal Society of London. Series A, Containing Papers of a Mathematical or Physical Character* 213(497-508) 437–456, ISSN 1364-503X, 1471-2962. doi:[10.1098/rsta.1914.0010](https://doi.org/10.1098/rsta.1914.0010)
69. Kolsky H (1949) An investigation of the mechanical properties of materials at very high rates of loading. In: *Proceedings of the physical society. Section B* 62(11):676–700, ISSN 0370-1301. doi:[10.1088/0370-1301/62/11/302](https://doi.org/10.1088/0370-1301/62/11/302)
70. Chen W W, Song B (2010) Split Hopkinson (Kolsky) bar: design, testing and applications. Springer, Berlin ISBN 978-1-4419-7982-7
71. Kalthoff JF (1988) Shadow optical analysis of dynamic shear fracture. *Opt Eng* 27(10):835–840. doi:[10.1117/12.797672](https://doi.org/10.1117/12.797672) ISSN 0091-3286
72. Meng Q, Wang Z (2015) Numerical simulation of loading edge cracks by edge impact using the extended finite element method. *Acta Mech Solida Sin* 28(2):156–167. doi:[10.1016/S0894-9166\(15\)30004-5](https://doi.org/10.1016/S0894-9166(15)30004-5) ISSN 0894-9166
73. Song J-H, Wang H, Belytschko T (2008) A comparative study on finite element methods for dynamic fracture. *Comput Mech*, 42(2) 239–250. ISSN 0178–7675, 1432–0924. doi:[10.1007/s00466-007-0210-x](https://doi.org/10.1007/s00466-007-0210-x)
74. Ha YD, Bobaru F (2010) Studies of dynamic crack propagation and crack branching with peridynamics. *Int J Fract*, 162(1–2) 229–244. ISSN 0376–9429, 1573–2673. doi:[10.1007/s10704-010-9442-4](https://doi.org/10.1007/s10704-010-9442-4)
75. Ramulu M, Kobayashi AS (1985) Mechanics of crack curving and branching— a dynamic fracture analysis. *Int J Fract*, 27(3–4) 187–201. ISSN 0376–9429, 1573–2673. doi:[10.1007/BF00017967](https://doi.org/10.1007/BF00017967)